LETTER

doi:10.1038/nature25155

One-pot growth of two-dimensional lateral heterostructures via sequential edge-epitaxy

Prasana K. Sahoo[1], Shahriar Memaran[2,3], Yan Xin[2], Luis Balicas[2,3] & Humberto R. Gutiérrez[1]

Two-dimensional heterojunctions of transition-metal dichalcogenides[1–15] have great potential for application in low-power, high-performance and flexible electro-optical devices, such as tunnelling transistors[5,6], light-emitting diodes[2,3], photodetectors[2,4] and photovoltaic cells[7,8]. Although complex heterostructures have been fabricated via the van der Waals stacking of different two-dimensional materials[2–4,14], the *in situ* fabrication of high-quality lateral heterostructures[9–13,15] with multiple junctions remains a challenge. Transition-metal-dichalcogenide lateral heterostructures have been synthesized via single-step[9,11,12], two-step[10,13] or multi-step growth processes[15]. However, these methods lack the flexibility to control, *in situ,* the growth of individual domains. *In situ* synthesis of multi-junction lateral heterostructures does not require multiple exchanges of sources or reactors, a limitation in previous approaches[9–13,15] as it exposes the edges to ambient contamination, compromises the homogeneity of domain size in periodic structures, and results in long processing times. Here we report a one-pot synthetic approach, using a single heterogeneous solid source, for the continuous fabrication of lateral multi-junction heterostructures consisting of monolayers of transition-metal dichalcogenides. The sequential formation of heterojunctions is achieved solely by changing the composition of the reactive gas environment in the presence of water vapour. This enables selective control of the water-induced oxidation[16] and volatilization[17] of each transition-metal precursor, as well as its nucleation on the substrate, leading to sequential edge-epitaxy of distinct transition-metal dichalcogenides. Photoluminescence maps confirm the sequential spatial modulation of the bandgap, and atomic-resolution images reveal defect-free lateral connectivity between the different transition-metal-dichalcogenide domains within a single crystal structure. Electrical transport measurements revealed diode-like responses across the junctions. Our new approach offers greater flexibility and control than previous methods for continuous growth of transition-metal-dichalcogenide-based multi-junction lateral heterostructures. These findings could be extended to other families of two-dimensional materials, and establish a foundation for the development of complex and atomically thin in-plane superlattices, devices and integrated circuits[18].

Chemical vapour deposition can produce high quality transition-metal dichalcogenide (TMD) monolayers and heterostructures[9–13]. The one-pot synthesis strategy involves using a single solid source, composed of MoX_2 and WX_2 powders placed within the same boat at high temperatures. Implementing this strategy for the fabrication of TMD-based heterostructures requires regulating the relative amounts of precursors in the gaseous phase through controlled vaporization from the solid sources, and/or promoting the selective deposition of individual compounds onto the substrate held at lower temperatures. In general, MX_2 compounds (where M = W, Mo and X = S, Se) have high dissociation temperatures. However, the presence of water vapour at high temperatures promotes the formation of highly volatile species, including metal oxides and hydroxides[16,17,19,20]. Using a one-pot strategy (Extended Data Fig. 1), we found that the selective growth of each TMD can be controlled independently, solely by switching the carrier gas (Extended Data Figs 2, 3): $N_2 + H_2O_{(g)}$ promotes the growth of MoX_2, whereas switching to $Ar + H_2$ (5%) stops the growth of MoX_2 and promotes the growth of WX_2. When the carrier gas is cyclically switched back and forth, heterostructures consisting of a sequence of multi-junctions can be synthesized continuously (Fig. 1 and Extended Data Fig. 4). The growth mechanism can be summarized as follows (see Methods and Extended Data Fig. 5 for a detailed discussion): $N_2 + H_2O_{(g)}$ (without H_2) favours the evaporation of both the molybdenum and the tungsten precursors (oxides and hydroxides), but because gaseous tungsten precursors are mainly hydroxides—which are volatile at temperatures above 500 °C (ref. 17)—only molybdenum precursors are deposited on the substrate. A sudden switch of the carrier gas to $Ar + H_2$ depletes the supply of molybdenum precursors, while supplying tungsten precursors owing to the slower reduction rate of WO_x. This vapour-phase modulation of the oxide species is the key driving force for the sequential growth of lateral heterojunctions.

Figure 1a–d shows optical images of a series of distinct multi-junction heterostructures, with alternating $MoSe_2$ (dark contrast) and WSe_2 (bright contrast) regions. The number of junctions is controlled by the number of gas-switching cycles, and the lateral size of each domain (width) is determined by the growth time of each individual cycle (Fig. 1 b, c and Extended Data Fig. 2a–h). The growth rate of $MoSe_2$ and WSe_2 domains was found to be a function of the substrate temperature (Extended Data Figs 1c, 2i). The single-crystalline heterostructure islands, up to 285 μm in size (Fig. 1a), are among the longest reported so far[10]. Spatially resolved Raman and micro-photoluminescence spectroscopies confirmed the sequential distribution of the chemical composition as well as the local optical properties within the heterostructures. Raman spectra (Fig. 1e) collected from regions 1 and 3 (Fig. 1a, inset) in the heterostructure exhibit the A_{1g} phonon mode (240 cm^{-1}) and the $E_{2g}{}^2$ (M) shear mode (shoulder at 249 cm^{-1}), corresponding to monolayer $MoSe_2$, whereas regions 2 and 4 display the A_{1g} (250 cm^{-1}) and the 2LA(M) (260 cm^{-1}) phonon modes of monolayer WSe_2 (refs 12, 21). Raman intensity maps at 240 cm^{-1} and 250 cm^{-1} further corroborated the spatial distribution of the $MoSe_2$ and WSe_2 domains, respectively (Extended Data Fig. 3c–f). The photoluminescence spectra (Fig. 1f) show a strong excitonic single peak at around 1.52 eV for $MoSe_2$ (regions 1 and 3) and 1.6 eV for WSe_2 (regions 2 and 4)[12]. The integrated photoluminescence intensity maps (Fig. 1g) and the corresponding composite map (Fig. 1h) of the heterostructures reveal the alternate formation of concentric triangular domains of $MoSe_2$ and WSe_2 monolayers (Extended Data Fig. 4a, c–e). The contour plots of the normalized photoluminescence intensity as a function of the position across three-junction (Fig. 1i) and five-junction (Fig. 1j) heterostructures clearly show the evolution of the distinct excitonic transitions within each domain. Across the first junction (marked 1), the $MoSe_2$ photoluminescence peak at 1.53 eV gradually shifts to higher energies until it reaches 1.60 eV, corresponding to the WSe_2 domain—a total shift of 70 meV. At the second and third junctions there is an abrupt

[1]Department of Physics, University of South Florida, Tampa, Florida 33620, USA. [2]National High Magnetic Field Laboratory, Florida State University, Tallahassee, Florida 32310, USA. [3]Department of Physics, Florida State University, Tallahassee, Florida 32306, USA.

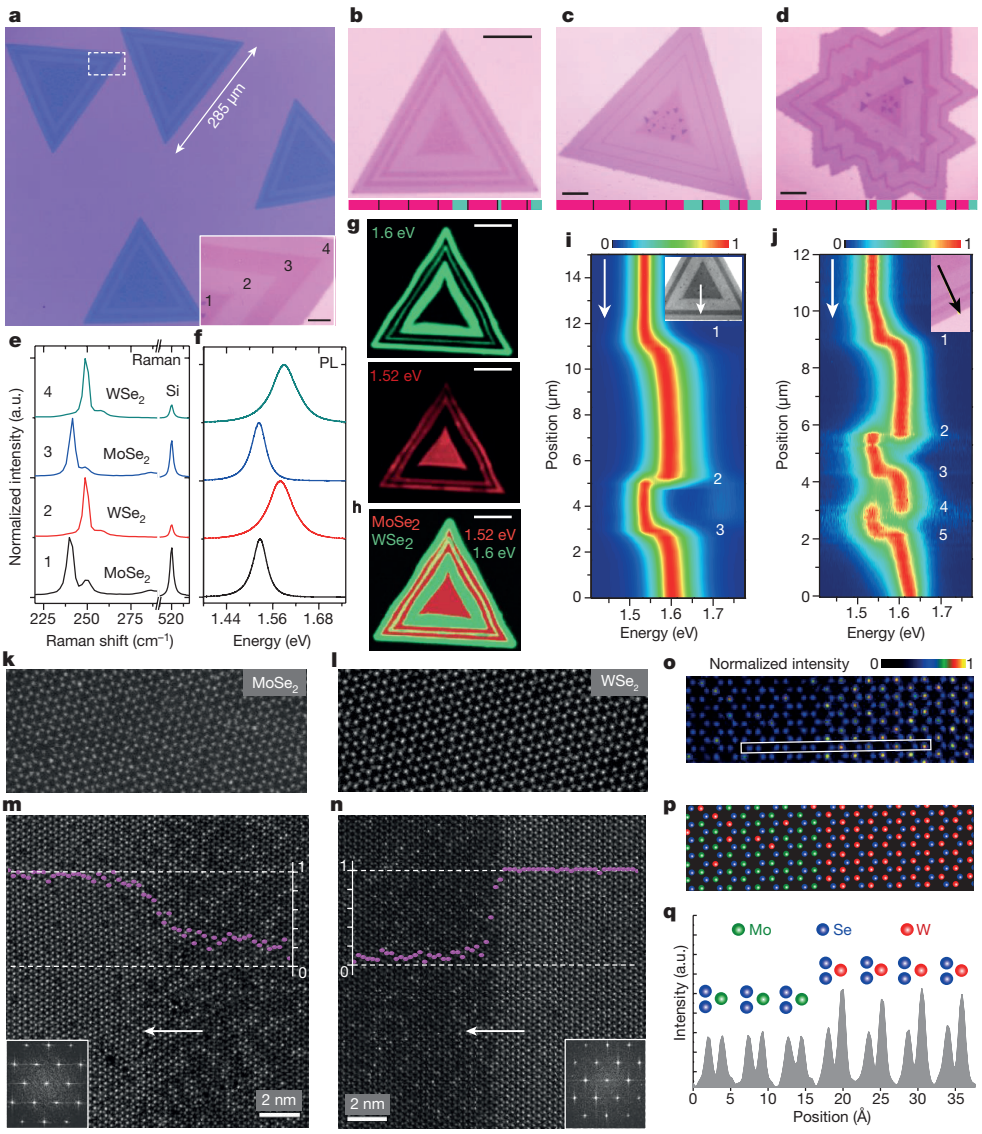

Figure 1 | Multi-junction lateral heterostructures and interfaces based on $MoSe_2$ and WSe_2. a, Low-magnification optical image of three-junction heterostructures. The inset shows a larger magnification of the area within the dashed box. The dark-contrast regions correspond to $MoSe_2$, the bright-contrast regions to WSe_2. **b**, **c**, Optical images of five-junction heterostructures. The difference in thickness of the $MoSe_2$ layers in **b** and **c** is seen by the difference in thickness of the dark-contrast regions. **d**, Seven-junction heterostructure with variable domain widths. The underlying colour bars in **b**–**d** depict the growth timescale: from left to right (pink, $MoSe_2$; green, WSe_2), each division (black line) corresponds to approximately 120 s. **e**, **f**, Raman (**e**) and photoluminescence (PL, **f**) spectra, of **a** at positions 1, 2, 3 and 4. **g**, **h**, Photoluminescence intensity maps for the WSe_2 (1.6 eV, top) and $MoSe_2$ (1.52 eV, bottom) domains (**g**), and composite photoluminescence map (**h**) for the heterostructure in **b**. **i**, **j**, Contour colour plots of the normalized photoluminescence intensity of three-junction (**i**) and five-junction (**j**) heterostructures, along the arrows in the insets. **k**, **l**, Z-contrast atomic-resolution HAADF-STEM images of pure $MoSe_2$ (**k**) and WSe_2 (**l**). **m**, **n**, Atomic-resolution HAADF-STEM images of the smooth (**m**) and sharp (**n**) interfaces, with their corresponding Fourier-transform patterns and composition profiles (atomic fraction of tungsten per vertical atomic column). The smooth and the sharp interfaces have average interface widths of 6 nm (21 atomic columns) and 1 nm (4 atomic columns), respectively. **o**, **p**, Scattered electron intensity colour plot (**o**) and associated atomic ball model (**p**) for the junction in **n**. **q**, Electron intensity profile along the white box in **i**. Scale bars, 10 μm (**a** (inset), **b**–**d**, **g**, **h**).

change in the position of the photoluminescence peak, suggesting the formation of sharper interfaces with less alloying. At these sharp interfaces, the photoluminescence spectra are characterized by an overlap of both peaks; this is due to the submicrometre laser spot size in the confocal microscope simultaneously probing both sides of the interface. Although junctions 2 and 3 are both sharper than junction 1, it is worth noting that junction 3 is not as sharp as junction 2; this behaviour has been consistently observed in all samples. It indicates that a transition from a $MoSe_2$ to a WSe_2 domain results in a less abrupt, slightly 'smoother' interface between the two materials, whereas the transition from a WSe_2 to a $MoSe_2$ domain produces atomically sharp interfaces. This was verified by atomic-resolution Z-contrast imaging using high-angle annular dark-field scanning transmission electron microscopy (HAADF-STEM) (Fig. 1k–o), which provides insight into both the crystalline quality and the chemical distribution at heterojunctions at a high spatial resolution. The atoms in monolayer $MoSe_2$ (Fig. 1k) and WSe_2 (Fig. 1l) have a hexagonal arrangement (honeycomb-like) with D_{3h} symmetry. The atomic positions of both Mo and Se_2 yield a similar intensity of scattered electrons, whereas the W sites display twice that intensity (Fig. 1q)[12]. Figure 1k, l shows pure $MoSe_2$ and WSe_2 regions, respectively, within the same heterostructure, confirming that the evaporation–deposition process is very selective even though both solid precursors (MSe_2 and WSe_2) are present in the heterogeneous source. Consistent with the photoluminescence observations, two types of interface were identified: $MoSe_2 \rightarrow WSe_2$ interfaces (Fig. 1m), which display a smooth, less abrupt chemical transition with some degree of alloy formation, and $WSe_2 \rightarrow MoSe_2$ interfaces, which are atomically sharp (Fig. 1n).

The different interfaces are a consequence of the different oxidation and reduction rates of molybdenum and tungsten compounds[22] as well as the gas switching mechanism. When the carrier gas switches from H_2O to H_2, the residual metal oxide content depletes rapidly. Because the complete replacement of H_2O to H_2 is not possible in the present experimental setup, this results in a small amount of co-deposition of Mo in the WX_2 domain, hence forming a smooth interface ($MoX_2 \rightarrow WX_2$). Under H_2 flow, while the WX_2 domain continues to grow, the molybdenum oxide(s) are converted completely to metallic molybdenum over the MoX_2 source. When the conditions are reversed—switching from H_2 to H_2O vapour again—the low-index W sub-oxides begin to form high-index W sub-oxides, as indicated by the slow weight-loss rate of the tungsten oxide precursor in H_2O (Extended Data Fig. 5c, d). Meanwhile, H_2O restores the initial oxidation step from metallic molybdenum—formed over MoX_2 during interaction with H_2 gas—to MoO_2, which is relatively slower than the direct oxidation of the MoX_2 source. This might lead to a delayed supply of MoO_2 vapour to the already present WX_2 edge-site, and hence result in a sharp transition from the WX_2 to the MoX_2 domain. Further optimization of the gas switching process could lead to the generation of sharp interfaces only.

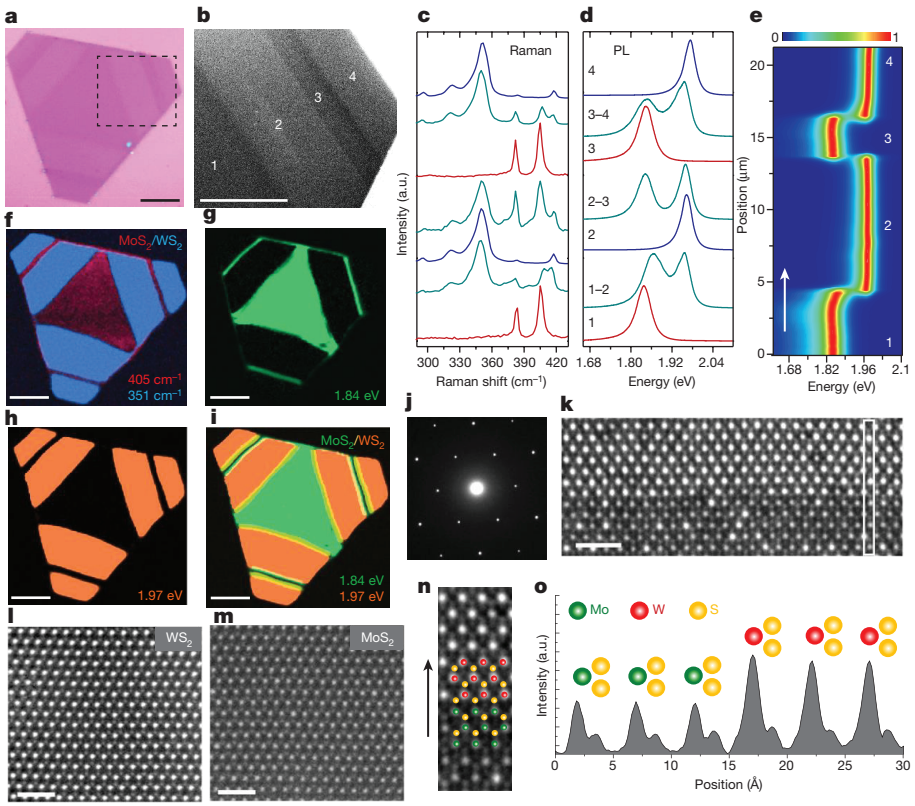

Figure 2 | Multi-junction lateral heterostructures based on MoS_2 and WS_2. **a**, Optical image of a heterostructure composed of three MoS_2–WS_2 junctions. **b**, SEM image of the region of the heterostructure within the dashed box in **a**. **c**, **d**, Raman (**c**) and photoluminescence (**d**) spectra at points 1, 2, 3, 4, and at the junctions 1–2, 2–3 and 3–4 indicated in **b**. **e**, Normalized photoluminescence colour contour plot along a direction perpendicular to the interfaces, where the white arrow indicates the growth direction. **f**, Composite Raman intensity map of the heterostructure. **g**, Photoluminescence intensity map of the MoS_2 domains, at 1.84 eV. **h**, Photoluminescence intensity map of the WS_2 domains, at 1.97 eV. **i**, Composite photoluminescence map of the heterostructure. **j**, Electron diffraction pattern of the heterostructure. **k**–**m**, Atomic-resolution HAADF-STEM images of a MoS_2–WS_2 interface (**k**), pure WS_2 (**l**) and pure MoS_2 (**m**) regions. **n**, Atomic ball model superimposed on the HAADF-STEM image of the interface. **o**, Electron intensity profile of the region along white box in **k**. Scale bars, 10 μm (**a**, **b**, **f**–**i**); 1 nm (**k**–**m**).

We further extended the use of the one-pot approach to produce sequential lateral heterostructures of sulfide monolayers (MoS_2–WS_2) (Extended Data Figs 6, 7). Figure 2a shows the optical image of a three-junction heterostructure (MoS_2–WS_2–MoS_2–WS_2). Its corresponding scanning electron microscopy (SEM) image (Fig. 2b) reveals the coexistence of alternating MoS_2 (dark contrast) and WS_2 (bright contrast) domains. The Raman spectra acquired at different positions (Fig. 2c), as well as the Raman maps (Fig. 2f), also confirm the sequential formation of MoS_2 and WS_2 domains. Regions 1 and 3 exhibit phonon modes at 384 cm^{-1} (E_{2g}) and 405 cm^{-1} (A_{1g}) that are consistent with monolayer MoS_2 (ref. 23), whereas the WS_2 regions (2 and 4) present the characteristic first-order (E^1_{2g} at 355 cm^{-1} and A_{1g} at 418 cm^{-1}) and second-order (most intense at 350 cm^{-1} (2LA(M)) Raman peaks[24]. At the interfaces (1–2, 2–3 and 3–4), the Raman spectra are mostly composed of a superposition of the vibrational modes of both MoS_2 and WS_2 domains (Supplementary Table 1). Single photoluminescence peaks associated with direct excitonic emissions from monolayers were observed for MoS_2 (1.84 eV) and WS_2 (1.97 eV) domains (Fig. 2d). The corresponding photoluminescence intensity maps at 1.84 eV (Fig. 2g), 1.97 eV (Fig. 2h) and composite image (Fig. 2i) show that, within each domain, the photoluminescence emission is homogeneous. The photoluminescence line scan across the junctions (Fig. 2e) also displays the modulation of the optical bandgap along the heterostructure with sharp discontinuities at the junctions. At the interfaces, the photoluminescence spectra show the superposition of two well-resolved peaks corresponding to the simultaneous excitation of MoS_2 and WS_2 domains. For the MoS_2→WS_2 interfaces 1–2 and 3–4, and around the MoS_2 domain, these photoluminescence peak positions are slightly blue-shifted by 25 meV and by 10 meV, respectively. Photoluminescence shifts were not observed at the WS_2 → MoS_2 interface (2–3), which is consistent with the results obtained for selenide-based junctions. Z-contrast images from the inner regions of each domain (Fig. 2l, m) confirm the high purity of the individual MoS_2 and WS_2 domains. The high quality and single-crystalline nature of these interfaces produced by lateral epitaxy was also verified by electron diffraction (Fig. 2j) and Z-contrast STEM imaging (Fig. 2k–o).

The morphology of the sulfide-based heterostructures involves MoS_2 cores with a truncated triangular geometry containing two types of zig-zag edge: metal-terminated (Mo-zz) and chalcogen-terminated (S-zz). The WS_2 domains grow preferentially along one of these MoS_2 edges, leading to WS_2 sections with a convex isosceles trapezoid shape. The consecutive MoS_2 growth follows the same pattern. The shape of the two-dimensional TMD crystal is determined by the relative growth rates of the different edges. Experimental[25] and theoretical[26] studies have shown that edge stability in MX_2 TMDs depends on the gas environment, the M:X atomic ratio and the growth temperature. A chalcogen-deficient environment promotes the formation of M-zz edges, while chalcogen-rich environments favour the stability of the X-zz edges. The distinct geometries observed in selenide- and sulfide-based heterostructures could originate from the different vaporization rates of selenium and sulfur, as well as the stability of the supply of the chalcogen atom during growth. This hypothesis is discussed in more detail in Methods.

TMD ternary alloys have received increasing attention owing to their composition dependent electronic properties and their potential to further expand the range of available two-dimensional materials beyond the four primary binary compounds (MoS_2, $MoSe_2$, WS_2 and WSe_2) (refs 27, 28). However, integrating different ternary alloys into a single crystal heterostructure has not yet been achieved. The versatility of the one-pot approach allowed us to fabricate sequential multi-junction heterostructures based on ternary alloys ($MoS_{2(1-x)}Se_{2x}$–$WS_{2(1-x)}Se_{2x}$). To this effect, solid sources containing combinations of either $MoSe_2$ + WS_2 or MoS_2 + WSe_2 were used. Figure 3a, b shows optical images of two distinct alloy-based lateral heterostructures (ALH1 and ALH2) with three junctions (Extended Data Figs 8–10). The corresponding photoluminescence maps (Fig. 3c, d) are consistent with different S:Se ratios. $MoS_{2(1-x)}Se_{2x}$ and $WS_{2(1-x)}Se_{2x}$ domains in ALH1 exhibit single photoluminescence peaks at 1.61 eV and 1.71 eV, respectively, whereas for ALH2 the Mo-rich and the W-rich domains have photoluminescence emissions at 1.67 eV and 1.8 eV, respectively. The photoluminescence line scan across ALH2 (Fig. 3e) shows that the position of the photoluminescence peak for each domain remains

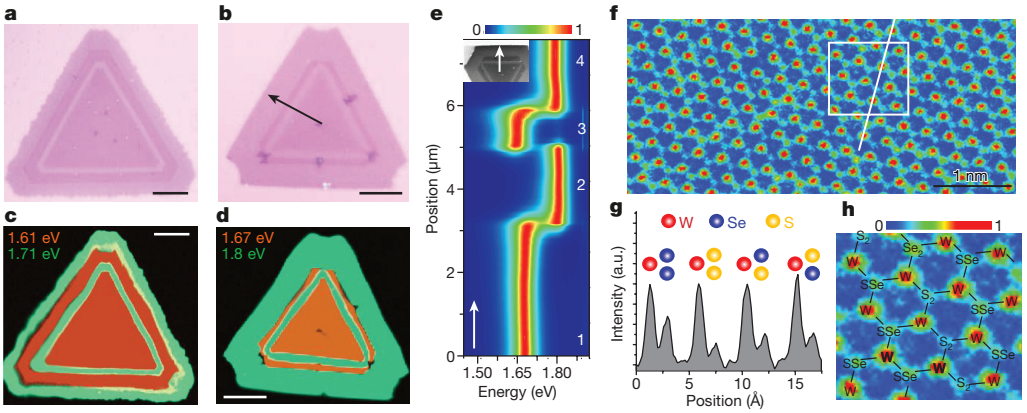

Figure 3 | Synthesis of three-junction lateral heterostructures based on MoX_2–WX_2. $X_2 = S_{2(1-n)}Se_{2n}$. **a**, **b**, Optical images of three-junction heterostructures composed of $MoS_{0.64}Se_{1.36}$–$WS_{0.68}Se_{1.32}$ (ALH1, **a**) and $MoS_{1.04}Se_{0.96}$–$WS_{1.08}Se_{0.92}$ (ALH2, **b**). **c**, **d**, Corresponding composite photoluminescence maps of ALH1 at 1.61 eV and 1.71 eV (**c**) and ALH2 at 1.6 eV and 1.8 eV (**d**). **e**, Normalized photoluminescence colour contour plot for ALH2 along a direction perpendicular to the interfaces; $\lambda_{exc} = 633$ nm. The inset shows a typical SEM image of ALH2; the width of the image corresponds to 24 μm. **f**, Atomic-resolution HAADF-STEM image of a $WS_{2(1-x)}Se_{2x}$ domain of ALH2. **g**, Electron intensity profile along the white line indicated in **f**. **h**, Magnified image of the region enclosed by the box in **f**, showing the different configurations of chalcogen sites. Scale bars, 10 μm (**a**–**d**).

constant, with sharp discontinuities at the interfaces. TEM analysis confirms that the individual domains are ternary alloys of $MoS_{2(1-x)}Se_2$ or $WS_{2(1-x)}Se_2$. Figure 3f shows a Z-contrast TEM image from a $WS_{2(1-x)}Se_{2x}$ domain. The differences in scattered electron intensities (Fig. 3g) associated with the metal sites (tungsten in this case) and with three distinct combinations of the chalcogen atoms (S_2, Se_2 or SSe) were used to identify the elemental configurations at the different atomic positions within the crystal[28] (Fig. 3h). The concentration (x) at each domain was calculated from the measured photoluminescence peak positions according to Vegard's law $E_g(MS_{2(1-x)}Se_{2x}) = (1-x)E_g(MS_2) + xE_g(MSe_2) - bx(1-x)$; where M = Mo or W and considering bandgap bowing parameters of $b = 0.05$

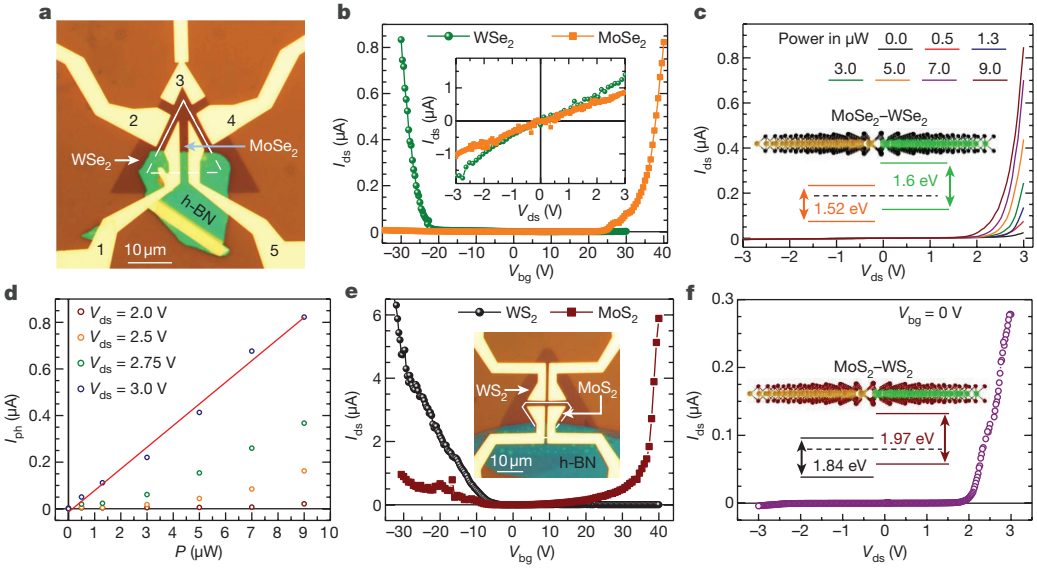

Figure 4 | Electrical characterization of the heterostructures. **a**, Micrograph of a $MoSe_2$–WSe_2 single junction grown by chemical vapour deposition, displaying the configuration of titanium and gold contacts used for the electrical characterization of the individual WSe_2 and $MoSe_2$ domains as well as the electrical transport across their junction. An exfoliated crystal of hexagonal boron nitride (h-BN) was transferred onto the lower edge of the junction to isolate contacts 1 and 5 from the WSe_2 edge, as these contacts are designed to probe only the $MoSe_2$ domain. The properties of the WSe_2 domain are probed through contacts 2 and 3 or 3 and 4. **b**, Typical drain to source current I_{ds} as a function of the gate voltage V_{bg} for the WSe_2 (green) and the $MoSe_2$ (orange) domains. The WSe_2 domain displays current mainly at negative gate voltages—that is, hole-doped-like transport—whereas the $MoSe_2$ domain displays an electron-doped-like response. The inset plots I_{ds} as a function of the bias voltage V_{ds}, showing a nearly linear dependence on V_{ds} when $V_{bg} = 0$ V. This indicates thermionic emission of charge carriers across the Schottky barriers located at the electrical contacts. **c**, I_{ds} as a function of V_{ds} across the $MoSe_2$–WSe_2 interface, displaying a typical diode-like response which becomes more prominent under illumination ($V_{bg} = 0$ V). The inset shows a sketch of the $MoSe_2$–WSe_2 domains, their interface, and respective band alignments. **d**, Photoinduced current $I_{ph} = I_{ds} - I_{dark}$, where I_{ds} is the current observed under illumination and I_{dark} is the current observed under dark conditions, as a function of the illumination power P. The red line is a linear fit, indicating a linear dependence of I_{ph} on P at high bias voltages. **e**, I_{ds} as a function of V_{bg} for a WS_2 (black) and a MoS_2 (brown) domain. Whereas WS_2 behaves as a hole-doped compound, MoS_2 displays ambipolar behaviour, albeit with a more pronounced electron-like response. The inset shows a micrograph of the MoS_2–WS_2 single junction device showing the configuration of contacts used to evaluate individual domains and their interface. **f**, I_{ds} as a function of V_{ds} across the MoS_2–WS_2 interface, showing the characteristic diode-like response. The inset shows a sketch of the MoS_2–WS_2 domains, their interface, and respective band alignments.

and $b = 0.04$ for the Mo-based and W-based alloys, respectively[29]. The calculated compositions for ALH1 are $MoS_{0.64}Se_{1.36}$ ($x = 0.68$) and $WS_{0.68}Se_{1.32}$ ($x = 0.66$). Similarly, compositions of $MoS_{1.04}Se_{0.96}$ ($x = 0.48$) and $WS_{1.08}Se_{0.92}$ ($x = 0.46$) were obtained for ALH2. Notably, a complete miscibility of S and Se was achieved for each individual $MoSe_{2(1-x)}S_{2x}$ and $WS_{2(1-x)}Se_{2x}$ domain, as the photoluminescence peak positions are constant within the domains. This is the first demonstration, to our knowledge, of the controlled synthesis of an alloy-based lateral heterostructure composed of multiple junctions.

Figure 4 displays a detailed electrical characterization of single junctions composed of $MoSe_2$ and WSe_2 domains, as well as MoS_2 and WS_2 domains, grown by chemical vapour deposition. For the different samples, we used distinct configurations of contacts allowing us to characterize the individual domains as well as the electrical transport across their interface (Fig. 4a). We find that the WSe_2 and WS_2 domains show a hole-doped-like response when contacted with gold on titanium, which is attributable to the Fermi level pinning close to their valence bands[30] (Fig. 4b, e). By contrast, the $MoSe_2$ and MoS_2 domains display a pronounced, electron-doped-like response given that gold on titanium is expected to pin the Fermi level closer to their conduction bands. Equally important is the fact that the current–voltage characteristics of, for example, the individual $MoSe_2$ and WSe_2 domains, display a nearly linear response (Fig. 4b, inset). This indicates that thermionic emission processes promote passage of the charge carriers across the misaligned bands of the semiconducting channel relative to those of the metallic contacts, or the Schottky barriers. That is, any nonlinearity observed for currents flowing across the $MoSe_2$–WSe_2 junction (Fig. 4c) cannot be attributed to these Schottky barriers. In fact, the current–voltage characteristics across the junction display a typical rectification or diode-like response, indicating the formation of a well-defined p–n junction. Additionally, as expected for a diode, illumination of the junction area leads to pronounced photoinduced currents (Fig. 4c, d). Figure 4e, f indicates that the MoS_2–WS_2 junctions show a similar overall response when compared to the $MoSe_2$–WSe_2 junctions; that is, a clear diode-like response or a well-defined p–n junction, although for this particular sample the current–voltage characteristics display a more pronounced nonlinearity. All domains show ON/OFF current ratios between 10^5 and 10^6 with relatively modest threshold gate voltages, that is inferior $V_{bg} = 10$ V when the I_{ds} as a function of V_{bg} is plotted in a logarithmic scale. This behaviour is comparable to that of samples fabricated from exfoliated single crystals, suggesting similar crystallinity.

The synthetic method developed here follows a different approach from previous methods, and is versatile and scalable. The continuous assembly of planar multi-junctions by a controlled sequential edge-epitaxy may allow for the realization of periodic one-dimensional quantum wells and planar superlattices. The controlled and sequential integration of alloy-based two-dimensional materials with tuned optical properties is another step forward, which could widen the range of possible material combinations for the design of spectral-selective two-dimensional heterogeneous materials for optoelectronic applications.

Online Content Methods, along with any additional Extended Data display items and Source Data, are available in the online version of the paper; references unique to these sections appear only in the online paper.

Received 15 June; accepted 10 November 2017.

1. Geim, A. K. & Grigorieva, I. V. Van der Waals heterostructures. *Nature* **499,** 419–425 (2013).
2. Withers, F. *et al.* Light-emitting diodes by band-structure engineering in van der Waals heterostructures. *Nat. Mater.* **14,** 301–306 (2015).
3. Xu, W. *et al.* Correlated fluorescence blinking in two-dimensional semiconductor heterostructures. *Nature* **541,** 62–67 (2017).
4. Yu, W. J. *et al.* Highly efficient gate-tunable photocurrent generation in vertical heterostructures of layered materials. *Nat. Nanotechnol.* **8,** 952–958 (2013).
5. Sarkar, D. *et al.* A subthermionic tunnel field-effect transistor with an atomically thin channel. *Nature* **526,** 91–95 (2015).
6. Lin, Y. C. *et al.* Atomically thin resonant tunnel diodes built from synthetic van der Waals heterostructures. *Nat. Commun.* **6,** 7311 (2015).
7. Pospischil, A., Furchi, M. M. & Mueller, T. Solar-energy conversion and light emission in an atomic monolayer p–n diode. *Nat. Nanotechnol.* **9,** 257–261 (2014).
8. Lee, C. H. *et al.* Atomically thin p–n junctions with van der Waals heterointerfaces. *Nat. Nanotechnol.* **9,** 676–681 (2014).
9. Duan, X. *et al.* Lateral epitaxial growth of two-dimensional layered semiconductor heterojunctions. *Nat. Nanotechnol.* **9,** 1024–1030 (2014).
10. Gong, Y. *et al.* Two-step growth of two-dimensional WSe_2/$MoSe_2$ heterostructures. *Nano Lett.* **15,** 6135–6141 (2015).
11. Gong, Y. *et al.* Vertical and in-plane heterostructures from WS_2/MoS_2 monolayers. *Nat. Mater.* **13,** 1135–1142 (2014).
12. Huang, C. *et al.* Lateral heterojunctions within monolayer $MoSe_2$–WSe_2 semiconductors. *Nat. Mater.* **13,** 1096–1101 (2014).
13. Li, M. Y. *et al.* Epitaxial growth of a monolayer WSe_2–MoS_2 lateral p–n junction with an atomically sharp interface. *Science* **349,** 524–528 (2015).
14. Kang, K. *et al.* Layer-by-layer assembly of two-dimensional materials into wafer-scale heterostructures. *Nature* **550,** 229–233 (2017).
15. Zhang, Z. *et al.* Robust epitaxial growth of two-dimensional heterostructures, multiheterostructures, and superlattices. *Science* **357,** 788–792 (2017).
16. Cannon, P. & Norton, F. J. Reaction between molybdenum disulphide and water. *Nature* **203,** 750–751 (1964).
17. Millner, T. & Neugebauer, J. Volatility of the oxides of tungsten and molybdenum in the presence of water vapour. *Nature* **163,** 601–602 (1949).
18. Wang, H. *et al.* Integrated circuits based on bilayer MoS_2 transistors. *Nano Lett.* **12,** 4674–4680 (2012).
19. Belton, G. R. & Jordan, A. S. The volatilization of molybdenum in the presence of water vapor. *J. Phys. Chem.* **69,** 2065–2071 (1965).
20. Belton, G. R. & McCarron, R. L. The volatilization of tungsten in the presence of water vapor. *J. Phys. Chem.* **68,** 1852–1856 (1964).
21. Nam, D., Lee, J. U. & Cheong, H. Excitation energy dependent Raman spectrum of $MoSe_2$. *Sci. Rep.* **5,** 17113 (2015).
22. Kilpatrick, M. & Lott, S. K. Reaction of flowing steam with refractory metals: III. Tungsten (1000°–1700°C). *J. Electrochem. Soc.* **113,** 17–18 (1966).
23. Lee, C. *et al.* Anomalous lattice vibrations of single- and few-layer MoS_2. *ACS Nano* **4,** 2695–2700 (2010).
24. Berkdemir, A. *et al.* Identification of individual and few layers of WS_2 using Raman spectroscopy. *Sci. Rep.* **3,** 1755 (2013).
25. Wang, S. *et al.* Shape evolution of monolayer MoS_2 crystals grown by chemical vapor deposition. *Chem. Mater.* **26,** 6371–6379 (2014).
26. Govind Rajan, A., Warner, J. H., Blankschtein, D. & Strano, M. S. Generalized mechanistic model for the chemical vapor deposition of 2D transition metal dichalcogenide monolayers. *ACS Nano* **10,** 4330–4344 (2016).
27. Duan, X. *et al.* Synthesis of $WS_{2x}Se_{2-2x}$ alloy nanosheets with composition-tunable electronic properties. *Nano Lett.* **16,** 264–269 (2016).
28. Feng, Q. *et al.* Growth of large-area 2D $MoS_{2(1-x)}Se_{2x}$ semiconductor alloys. *Adv. Mater.* **26,** 2648–2653 (2014).
29. Kang, J., Tongay, S., Li, J. B. & Wu, J. Q. Monolayer semiconducting transition metal dichalcogenide alloys: Stability and band bowing. *J. Appl. Phys.* **113,** 143703 (2013).
30. Pradhan, N. R. *et al.* Hall and field-effect mobilities in few layered *p*-WSe_2 field-effect transistors. *Sci. Rep.* **5,** 8979 (2015).

Supplementary Information is available in the online version of the paper.

Acknowledgements This work was supported by the National Science Foundation (NSF) grant DMR-1557434 (CAREER: Two-Dimensional Heterostructures Based on Transition Metal Dichalcogenides). L.B acknowledges the US Army Research Office MURI grant W911NF-11-1-0362 (Synthesis and Physical Characterization of Two-Dimensional Materials and Their Heterostructures) and the Office Naval Research DURIP Grant 11997003 (Stacking Under Inert Conditions). TEM work was performed at the National High Magnetic Field Laboratory, which is supported by the NSF Cooperative Agreement DMR-1157490 and the State of Florida. P.K.S. and H.R.G. thank M. A. Cotta for comments.

Author Contributions P.K.S. and H.R.G. conceived the idea and designed the experiments. P.K.S. performed the synthesis, Raman and photoluminescence characterization, and related analysis. S.M. and L.B. performed device fabrication, electrical measurements and analysis. Y.X. conducted aberration-corrected STEM imaging with assistance from P.K.S. and H.R.G. H.R.G. carried out TEM data analysis. P.K.S. and H.R.G. analysed the results and wrote the paper with input from L.B., S.M. and Y.X. All authors discussed the results and commented on the manuscript. H.R.G. supervised the project.

Author Information Reprints and permissions information is available at www.nature.com/reprints. The authors declare no competing financial interests. Readers are welcome to comment on the online version of the paper. Publisher's note: Springer Nature remains neutral with regard to jurisdictional claims in published maps and institutional affiliations. Correspondence and requests for materials should be addressed to H.R.G. (humberto3@usf.edu) or P.K.S. (prasanasahoo@gmail.com).

Reviewer Information *Nature* thanks Q. Xiong and the other anonymous reviewer(s) for their contribution to the peer review of this work.

METHODS

Synthesis. All in-plane lateral heterostructures were synthesized by water-assisted thermal evaporation from solid sources at atmospheric pressure, in a chemical vapour deposition system developed in-house. Bulk powders of $MoSe_2$ (99.9%, Sigma-Aldrich), WSe_2 (99.9%, Sigma-Aldrich) MoS_2 (99.9%, Sigma-Aldrich) or WS_2 (99.9%, Sigma-Aldrich) were used directly in different combinations for the synthesis of, mainly, four types of heterostructures: $MoSe_2$–WSe_2 (150 mg); MoS_2–WS_2 (150 mg); $MoSe_{0.96}S_{1.04}$–$WSe_{0.92}S_{1.08}$ ($MoSe_2$–WS_2 (150 mg)); $MoS_{0.64}Se_{1.36}$–$WSe_{1.32}S_{0.68}$ (MoS_2–WSe_2 (150 mg)). For the growth of MoX_2–WX_2 (where X = S, Se), powder sources containing MoX_2 and WX_2 in a ratio of 2:1 were placed side-by-side within an alumina boat (L × W × H: 70 × 14 × 10 mm) in the centre of a 1-inch diameter horizontal quartz tube furnace. Si substrates, with a 300 nm SiO_2 layer, were pre-cleaned with acetone, isopropanol and deionized water. During the growth, the substrates were placed downstream at temperatures between 810 and 700 °C, 6–10 cm away from the solid sources at 1,060 °C. Initially, the temperature of the furnace was slowly raised to 1,060 °C over 50 min with a constant flow of N_2 (200 standard cubic centimetres per minute, s.c.c.m.) and both substrates and sources were kept outside the furnace. When the temperature of the furnace reached greater than 1,040 °C, the solid precursor and the substrates were moved to their respective positions, by sliding the quartz tube into the furnace, and simultaneously water vapour was introduced in a controlled manner by diverting N_2 flow through a bubbler (Sigma-Aldrich) containing 2 ml of deionized water at room temperature. In order to switch the growth from Mo-rich to W-rich compounds, resulting in a lateral heterostructure, the $N_2 + H_2O$ vapour flux was rapidly replaced by a mixture of Ar + 5% H_2 (200 s.c.c.m.). Similar growth conditions were employed for the growth of heterostructures with other compositions. Once the desired heterostructure sequence was completed, the synthesis process was abruptly terminated by sliding the quartz tube containing both the precursor and substrates to a cooler zone, while keeping a 200 s.c.c.m. constant flow of Ar + H_2 (5%) until it cooled to room temperature.

Raman and photoluminescence spectroscopy. The Raman and photoluminescence experiments were performed in a confocal microscope-based Raman spectrometer (LabRAM HR Evolution, Horiba Scientific) in backscattering geometry. Excitation wavelengths of 532 nm and 632 nm (laser power at the sample, 77 μW), focused with a 100× objective (numerical aperture 0.9, working distance 0.21 mm). During the photoluminescence and Raman mapping the optical path is stationary, while moving the sample on a computer controlled motorized XY stage.

Transmission electron microscopy. HAADF-STEM imaging was carried out on an aberration-corrected JEOL JEM-ARM200cF with a cold-field emission gun at 200 kV. The STEM resolution of the microscope is 0.78 Å. The HAADF-STEM images were collected with the JEOL HAADF detector using the following experimental conditions: probe size 7c, condenser lens aperture 30 μm, scan speed 32 μs per pixel, and camera length 8 cm, which corresponds to a probe convergence angle of 21 mrad and inner collection angle of 76 mrad.

Device fabrication. To fabricate the electrical contacts to individual layers within MoX_2 and WX_2 domains, 80 nm of gold were deposited onto an 8 nm thick layer of titanium via e-beam evaporation. Contacts were patterned using standard e-beam lithography techniques. After gold deposition, and in order to extract adsorbates, the samples were annealed under high vacuum for 24 h at 120 °C. In the case of WSe_2–$MoSe_2$ heterojunctions, before deposition, approximately 30 nm of hexagonal boron nitride crystals (Momentive PolarTherm PT110) were mechanically exfoliated from larger crystals, and transferred onto the heterostructure using a similar technique to that described in ref. 8.

Electrical characterization. Electrical characterization experiments were performed using a source meter (Keithley 2612 A). The sourcemeter was controlled via Labtracer2, free software available at https://www.tek.com/source-measure-units/2400-c-software/labtracer-28-unsupported. For photocurrent measurements, a Coherent Sapphire 532-150 CW CDRH and Thorlabs DLS146-101S were used, with a continuous wavelength λ of 532 nm. Light was transmitted to the sample through a 10-μm single-mode optical-fibre with a mode field diameter of 10 μm. The size of the laser spot was also measured against a fine grid. An I_0 value of the order of 10^{-12} A yields diode ideality factors ranging from approximately 3.2 to 4.5, while yielding reasonable values for the shunt resistance R_s, that is between approximately 2.5 and 4.5 MΩ. We find that good fits are obtained when I_0 is allowed to decrease to values below the noise floor of the measurements, approaching at least 10^{-15} A. This uncertainty in the value of I_0 has no effect on the values of f or R_s. The diode-like electrical responses were fitted using the Shockley diode equation in the presence of a series resistor R_s (ref. 8): $I_{ds} = \frac{nV_T}{R_s} W_0\left\{\frac{I_0 R_s}{fV_T}\exp\left(\frac{V_{ds}+I_0R_s}{fV_T}\right)\right\} - I_0$, where V_T is the thermal voltage at a temperature T, I_0 is the reverse bias current, f is the diode ideality factor ($f = 1$ for an ideal diode) and $W_0\{x\}$ is the Lambert function. The results of the electrical characterization experiments are shown in Fig. 4 in detail.

Growth mechanism. A preliminary study was performed to evaluate the interaction mechanism between water vapour and MoX_2 as well as WX_2 bulk powders. By allowing the solid precursor to interact with water vapour at 1,060 °C for a prolonged time (at least 20–30 min), it was found that different Mo (or W) oxide phases evolve, which are assumed to be the main driving force behind the selective growth of the individual compounds. It can be seen clearly from the Raman spectra (Extended Data Fig. 5a) that MoO_2 is the dominant phase evolving during the oxidation of MoS_2 or of $MoSe_2$. The Raman peak position of the partially oxidized cluster shows the presence of both $MoSe_2$ (or MoS_2) and MoO_2 phases, whereas from completely oxidized domains, only frequencies at 126, 203, 228, 347, 363, 458, 496, 570 and 742 cm^{-1} were observed; this agrees well with the Raman spectra of MoO_2 (ref. 31). A previous report also confirmed that the main solid product during MoS_2 oxidation under water vapour at temperatures greater than 1,000 °C is MoO_2 (ref. 32) rather than MoO_3, which tends to be a stable phase under various reactive gas environments[33]. Indeed, in our experiments, the overall oxidation reaction between MoX_2 and water at 1,060 °C led to the formation of MoO_2 (reaction (1)). Furthermore, it was found that the weight loss of Mo-oxides is very rapid in the presence H_2O vapour (Extended Data Fig. 5c). Taking this into account, presumably, the sublimation of MoO_2 proceeds very rapidly at a temperature of 1,060 °C, and subsequently the vapour is transported and saturated on the desired substrate at relatively lower temperatures[34]. The recondensed MoO_2 vapour interacts with the H_2X already present (as a by-product of oxidation) to form MoX_2 at temperatures ranging from 650 to 800 °C (reaction (2))[34,35]. This leads to the formation of MoX_2 domains. Notably, the growth of MoX_2 can be abruptly terminated by changing the carrier gas from wet nitrogen to dry argon with 5% hydrogen, which rapidly depletes the source of MoO_2 vapours owing to its reduction by hydrogen to metallic molybdenum at the surface of the source (reaction (3)). Unfortunately, the detection of the exact transport phases was not possible because of constrained access to the reaction tube of the chemical vapour deposition system under the conditions used for the growth of the TMD heterostructures. Therefore, only the most important reaction equations were derived:

$$MoX_{2(s)} + 4H_2O_{(g)} \rightarrow MoO_{2(s)} + H_2X_{(g)} + XO_{2(g)} + 3H_{2(g)}, \text{ where X = S or Se} \quad (1)$$

$$MoO_{2(g)} + 2H_2X_{(g)} \rightarrow MoX_{2(s)} + 2H_2O_{(g)}, \text{ where X = S or Se} \quad (2)$$

$$MoO_{2(s)} + 2H_{2(g)} \rightarrow Mo_{(s)} + 2H_2O_{(g)} \quad (3)$$

By contrast, WX_2 has different oxidation and reduction behaviour (Extended Data Fig. 5c, d) under the above conditions, in which different W_xO_y oxide phases are observed in the Raman spectra (Extended Data Fig. 5b) and Supplementary Table 2. In the case of WSe_2, distinct oxide phases evolved upon reaction with different reactive gas vapours for more than 20 min at 1,060 °C, as shown in Extended Data Fig. 5b[36–38]. The dominant phases observed in the Raman spectra are WO_2 (refs 36, 38, 39) and $W_{20}O_{58}$ (ref. 37). This indicates that the oxidation state of W is dominated by that within WO_2 and $W_{20}O_{58}$ during the oxidation reaction of WX_2 in wet nitrogen carrier gas by a series of reaction steps (reactions (4)–(7)):

$$WX_{2(s)} + 4H_2O_{(g)} \rightarrow WO_{2(s)} + H_2X_{(g)} + XO_{2(g)} + 3H_{2(g)}, \text{ where X = S or Se} \quad (4)$$

$$18WO_{2(s)} + 12H_2O_{(g)} \rightarrow W_{18}O_{48(s)} + 12H_{2(g)} \quad (5)$$

$$W_{18}O_{48(s)} + 10H_2O_{(g)} \rightarrow W_{20}O_{58(s)} + 10H_{2(g)} \quad (6)$$

$$\frac{1}{20}W_{20}O_{58(s)} + 2H_2O_{(g)} \rightarrow WO_3{\cdot}n(H_2O) + 10H_{2(g)}, \text{ where } n = 0\text{–}1 \quad (7)$$

The formation of any volatile $WO_3{\cdot}(H_2O)$ or similar tungstate species in $N_2 + H_2O$ vapour cannot be ruled out, however these species mostly condense below 500 °C[40] and hence might not be participating in the growth process. Similarly, in the presence of the reducing agent H_2, the high-index W sub-oxides undergo a series of phase transformations to low-index oxide phases (reactions (8)–(10))[34,41]:

$$W_{20}O_{58(s)} + 10H_{2(g)} \rightarrow W_{18}O_{48(s)} + 10H_2O_{(g)} \quad (8)$$

$$W_{18}O_{48(s)} + H_{2(g)} \rightarrow 18WO_{2(s)} + 12H_2O_{(s)} \quad (9)$$

$$\frac{3}{2}WO_{2(s)} \rightarrow \frac{1}{n}(WO_3)_{n(g)} + \frac{1}{3}W_{(g)} \quad (10)$$

The different $(WO_3)_{n(g)}$ species can be formed alongside the reduction process, and subsequently transported as vapour to the growth substrate (reaction (11)); the reaction of WO_2 is shown as reaction (12):

$$(WO_3)_{n(g)} + 2\,H_2X_{(g)} \rightarrow WX_{2(s)} + 2\,H_2O_{(g)},\ \text{where X = S or Se} \quad (11)$$

or

$$WO_{2(g)} + 2\,H_2X_{(g)} \rightarrow WX_{2\,(s)} + 2H_2O_{(g)},\ \text{where X = S or Se} \quad (12)$$

Reactions (8)–(10) and (11)–(12) can occur concurrently. The appearance of different molybdenum and tungsten oxidation states can also be directly observed from the colour changes of the solid precursors after exposure to different gaseous environments: MoO_2 (brown), $W_{20}O_{58}$ (blue), a violet colour indicating the presence of $W_{20}O_{58}$ and $W_{18}O_{49}$ phases in a whisker-type morphology[42] and WO_2 (chocolate brown) (Extended Data Fig. 5e–l).

There are important differences in the behaviour of molybdenum and tungsten-based compounds in the presence of water vapour[22]. Firstly, the oxide products of tungsten are relatively less volatile than those of the corresponding molybdenum compounds. In addition, the high-index W sub-oxides ($W_{20}O_{58}$) are less volatile and less readily oxidized to WO_3. This vapour-phase modulation of the oxide species is the key driving force for the observed sequential growth of lateral heterostructures. Thus, the growth mechanism can be summarized as follows. The selective growth of MoX_2 or WX_2 monolayers can be achieved simply by controlling the carrier gas environment. $N_2 + H_2O$ vapour (without H_2) favours the evaporation of both molybdenum and tungsten precursors, but only molybdenum precursors are deposited on the substrate. An abrupt switch of the carrier gas to $Ar + H_2$ quickly depletes the supply of molybdenum precursors, while continuing to supply tungsten precursors owing to the slower reduction rate of WO_x. A more detailed chemical analysis, including the type of gaseous by-products, in conjunction with theoretical models is ongoing.

In order to further understand the role of molybdenum or tungsten oxides during the switching of one material domain to the other (such as MoX_2 to WX_2), and the extent of material diffusion across the interface while changing the carrier gas from $N_2 + H_2O$ to $Ar + H_2$ for heterostructure fabrication, the oxidation induced evaporation and the rapid reduction behaviour of different solid sources, including MoO_3 and WO_3, were evaluated independently at 1,060 °C (Extended Data Fig. 5c, d).

Case 1, in the presence of H_2O. It can be seen from Extended Data Fig. 5c that sublimation of MoO_3 is almost instantaneous (97% weight loss in 2 min). By contrast, the sublimation of WO_3 is very slow (approximately 2% weight loss in 2 min) and is linear. This is further supported by the observation that the weight loss of $MoSe_2$ is around three times higher than that of WSe_2 for a 10-min interaction with H_2O, which is otherwise linear. This shows that, in the presence of H_2O, the Mo-oxide vapours dominate over W-oxide vapours in the reaction zone. It can be concluded that, in the presence of water vapour, oxide products of tungsten are relatively less volatile than the corresponding molybdenum compounds. In fact, the slower oxidation of tungsten compounds might aid the formation of tungsten oxide hydroxide ($WO_3{\cdot}xH_2O$) species, which generally condense below 500 °C. Hence, an H_2O environment favours the growth of only MoX_2 domains.

Case 2, in the presence of H_2 reducing gas. MoO_3 undergoes rapid phase transformation to different sub-oxide phases until it is completely reduced to Mo, via the steps $MoO_3 \rightarrow Mo_4O_{11} \rightarrow MoO_2 \rightarrow Mo$ (Supplementary Table 3)[43]. A weight loss of around 75% was observed in 10 min. In a similar time frame, however, WO_3 undergoes a linear transformation to different sub-oxide phases via $WO_3 \rightarrow W_nO_{3n-1} \rightarrow W_nO_{3n-2}$ ($W_{20}O_{58}$) $\rightarrow W_{18}O_{48} \rightarrow WO_2$ (Supplementary Table 3). A maximum weight loss of 8.5% was observed in 10 min, which is almost 9 times slower than the reduction process of MoO_3. It indicates that, during the switching of H_2O to H_2 carrier gas, the residual MoO_2 reduces instantaneously; however, the supply of W sub-oxides is maintained. In addition, the leaching of W sub-oxides by H_2 is more rapid than their rate of reduction to lower W sub-oxides, thus contributing to the growth of the WSe_2 domain.

From the above observation, it can be concluded that H_2O vapour favours the growth of the $MoSe_2$ domain because the population of molybdenum oxides dominates the reaction chamber. The rapid reduction of MoO_3 indicates (Extended Data Fig. 5d) that the rate of $MoSe_2$ oxidation is equal to the rate of MoO_2 sublimation, meaning that all the MoO_2 oxide formed during the interaction of H_2O with $MoSe_2$ sublimes instantly. This has been further confirmed during the oxidation of $MoSe_2$, in which we do not encounter any signatures of higher Mo-oxide phases. On the other hand, H_2O vapour favours the continuous oxidation of the WSe_2 precursor to higher sub-oxide phases of W, and the typical timescale of growth of the $MoSe_2$ domain does not apply in this case. However, any higher W sub-oxides that occur during WSe_2 oxidation, such as $W_{20}O_{58}$ or WO_3, can effectively capture an H_2O molecule and form tungsten oxide hydroxide ($WO_3{\cdot}H_2O$), which is very volatile and hence can only condense below 500 °C. The different interfaces during the transition from one material to other are a consequence of the different oxidation and reduction rates of molybdenum and tungsten-based compounds as well the gas switching mechanism. When the carrier gas switches from H_2O to H_2 (as a reducing agent), the residual Mo-oxide content depletes suddenly, as observed from the weight-loss plot. Because, in the present experimental setup, absolute depletion of H_2O to H_2 is not possible, this resulted in a mild co-deposition of Mo into the WX_2 domain, hence forming a smooth interface ($MoX_2 \rightarrow WX_2$). Note that, during the continuous growth of the WX_2 domain, the Mo-oxide completely depletes into metallic molybdenum over the MoX_2 source. When the condition is reverted—that is, changing from H_2 to H_2O vapour—the W sub-oxides proceed towards forming high-index W sub-oxides, as indicated by the slow weight-loss of W-oxide precursors in H_2O. Meanwhile, H_2O restores the initial oxidation step from metallic molybdenum that, during the interaction with H_2 gas, formed at the MoX_2 surface. This forms MoO_2 relatively more slowly than the direct oxidation of the MoX_2 source. This might result in a slight delay to the supply of MoO_2 vapour to the already existing WX_2 edge-site, and hence always results in a sharp transition from the WX_2 to the MoX_2 domain.

Assignment of Raman modes of $MoS_{0.64}Se_{1.36}$–$WSe_{1.32}S_{0.68}$ lateral heterostructure. The compositional and spatial distribution of (S–Se) alloy in the $MoS_{2(1-x)}Se_{2x}$–$WS_{2(1-x)}Se_{2x}$ lateral heterostructures were examined using Raman measurements (Fig. 3a, b and Extended Data Figs 8, 10). The normalized Raman spectra in Extended Data Fig. 8c indicate that the MoX_2- and WX_2-related Raman branches are well separated, and mostly consist of several intense peaks in the range of 100 to 500 cm^{-1}. The intense Raman peaks (Extended Data Fig. 8c) observed within domains 1 and 3 (Extended Data Fig. 8a) are related to an alloy phase of $MoS_{2(1-x)}Se_{2x}$ (refs 28, 44). In general, A_{1g} and E_{2g} modes in monolayer $MoS_{2(1-x)}Se_{2x}$ show typical two-mode behaviour and do not imply phase segregation[44]. Splitting of the A_{1g} mode has also been observed, which is attributed mainly to the mass difference between Se and S as well as their spatial configuration around Mo atoms[44]. Hence, the observed Raman spectra (Extended Data Fig. 8c) for the $MoS_{2(1-x)}Se_{2x}$ monolayer domains have two distinct sets of features: MoS_2-like features ($E_{2g(S-Mo)}$ (370 cm^{-1}) and $A_{1g(S-Mo)}$ modes (400.5 cm^{-1})), and $MoSe_2$-like features close to 264 cm^{-1}. In detail, the peaks at 219 cm^{-1} and 264 cm^{-1} are observed as a result of A_{1g} mode splitting of the $MoSe_2$ phase into low and high-frequency domains, respectively, whereas MoS_2-like A_{1g} shifts from 405 to 400.5 cm^{-1}, and E_{2g} shifts from 385 to 370 cm^{-1}, confirm the presence of Se incorporation in the lattice site of S (ref. 45). Similarly, the normalized Raman spectra corresponding to domains 2 and 4 (Extended Data Fig. 8a) display several phonon modes typical of a $WSe_{2x}S_{2(1-x)}$ alloy, which can be assigned to modes $A_{1g(Se-W)}$ (256–259 cm^{-1}), $A_{1g(S-W)}$ (404–406 cm^{-1}), $A_{1g(S-W-Se)}$ (379–381 cm^{-1}), $E_{2g(S-W)}$ (354 cm^{-1}), A_{1g}(m)-$LA_{(S-W)}$ (225 cm^{-1}) and $A_{1g(Se-W)}$–$LA_{(Se-W)}$ + $E_{2g(S-W)}$–$LA_{(S-W)}$ (138–141 cm^{-1}) (ref. 27). The observed red shift (around 12 cm^{-1}) of the $A_{1g(S-W)}$ mode in a Se-rich environment, as compared to that of isotropic monolayer WS_2 phase and the corresponding hardening of the $A_{1g(Se-W)}$ mode, clearly indicates the presence of Se/S alloy in $MoS_{2(1-x)}Se_{2x}$ and $WS_{2(1-x)}Se_{2x}$ domains. However, the position of the $E_{2g(S-W)}$ mode does not change (±1 cm^{-1}), which might be attributed to the weak coupling between the very weak $E_{2g(Se-W)}$ mode and the strong $E_{2g(S-W)}$ mode[27]. This has been further confirmed by Raman intensity mapping as shown in the composite image (individual component maps in Extended Data Fig. 8h–k). Even though the $A_{1g(S-W)}$ and $A_{1g(S-Mo)}$ peaks differ by only around 4 cm^{-1}, the mapping provides clear in-plane differentiation between these two domains that matches the optical contrast of the heterostructure.

Assignment of Raman modes of $MoSe_{0.96}S_{1.04}$–$WSe_{0.92}S_{1.08}$ lateral heterostructure. Extended Data Fig. 10b shows the $MoSe_{2(1-x)}S_{2x}$ and $WS_{2(1-x)}Se_{2x}$ related Raman spectra at different regions of the heterostructure (including the junctions) corresponding to the optical image in Fig. 3b. The prominent peaks, observed within domain 1 and 3 (Extended Data Fig. 10a), are mostly related to an alloy phase of $MoSe_{2(1-x)}S_{2x}$, which can be assigned to MoS_2-like peaks ($A_{1g(S-Mo)}$ modes (402.5 cm^{-1}), $E_{2g(S-Mo)}$ (371–374 cm^{-1})) and $MoSe_2$-like peaks (high frequency $A_{1g(Se-Mo)}$ modes (266–267 cm^{-1}), low frequency $A_{1g(Se-Mo)}$ modes (223 cm^{-1}), and $E_{2g(Se-Mo)}$ (277–278 cm^{-1})). Similarly, Raman spectra collected from domains 2 and 4 display several modes that correspond to a typical $WS_{2(1-x)}Se_{2x}$ alloy, and can be assigned to modes $A_{1g(S-W)}$ (211–213 cm^{-1}), $A_{1g(Se-W)}$ (263 cm^{-1}), $E_{2g(S-W)}$ (around 356–358 cm^{-1}), A_{1g}(m)-$LA_{(S-W)}$ (around 225 cm^{-1}) and $A_{1g(Se-W)}$-$LA_{(Se-W)}$ + $E_{2g(S-W)}$-$LA_{(S-W)}$ (around 160 cm^{-1}). The $A_{1g(S-W)}$ mode is red shifted by approximately 4 cm^{-1}, whereas the corresponding large shift of the $A_{1g(Se-W)}$ mode is due to the occurrence of uniform S/Se alloying in these heterostructures. This is supported by the distinct photoluminescence spectra (Extended Data Fig. 10c, d) collected from the $MoSe_{2(1-x)}S_{2x}$ and $WS_{2(1-x)}Se_{2x}$ domains. The individual Raman and photoluminescence maps further confirm the seamless connectivity as well as uniformity in the distribution of S/Se alloy within the triangular domains (Extended Data Fig. 10).

Data availability. The datasets generated and/or analysed in the current study are available from the corresponding authors upon reasonable request, and are also included with the manuscript as Extended Data and Supplementary Information.

31. Spevack, P. A. & McIntyre, N. S. Thermal reduction of MoO_3. *J. Phys. Chem*. **96,** 9029–9035 (1992).
32. Blanco, E., Sohn, H. Y., Han, G. & Hakobyan, K. Y. The kinetics of oxidation of molybdenite concentrate by water vapor. *Metall. Mater. Trans. B* **38,** 689–693 (2007).
33. Walter, T. N., Kwok, F., Simchi, H., Aldosari, H. M. & Mohney, S. E. Oxidation and oxidative vapor-phase etching of few-layer MoS_2. *J. Vac. Sci. Technol. B* **35,** 021203 (2017).
34. Blackburn, P. E., Hoch, M. & Johnston, H. L. The vaporization of molybdenum and tungsten oxides. *J. Phys. Chem*. **62,** 769–773 (1958).
35. Kadiev, K. M., Gyul'maliev, A. M., Shpirt, M. Y. & Khadzhiev, S. N. Thermodynamic and quantum chemical study of the transformations and operation mechanism of molybdenum catalysts under hydrogenation conditions. *Petrol. Chem*. **50,** 312–318 (2010).
36. Frey, G. L. *et al.* Investigations of nonstoichiometric tungsten oxide nanoparticles. *J. Solid State Chem*. **162,** 300–314 (2001).
37. Chen, J. *et al.* Synthesis and Raman spectroscopic study of $W_{20}O_{58}$ nanowires. *J. Phys. D* **41,** 115305 (2008).
38. Lu, D. Y., Chen, J., Deng, S. Z., Xu, N. S. & Zhang, W. H. The most powerful tool for the structural analysis of tungsten suboxide nanowires: Raman spectroscopy. *J. Mater. Res.* **23,** 402–408 (2008).
39. Rothschild, A., Frey, G. L., Homyonfer, M., Tenne, R. & Rappaport, M. Synthesis of bulk WS_2 nanotube phases. *Mater. Res. Innov*. **3,** 145–149 (1999).
40. Smolik, G. R., Petti, D. A., McCarthy, K. A. & Schuetz, S. T. *Oxidation, Volatilization, and Redistribution of Molybdenum from TZM Alloy in Air*. Report No. INEEL/EXT-99-01353 (Idaho National Engineering and Environmental Laboratory, 2000).
41. Taskinen, P., Hytonen, P. & Tikkanen, M. H. On the reduction of tungsten oxides. II. *Scand. J. Metall*. **6,** 228–232 (1977).
42. Sarin, V. K. Morphological changes occurring during reduction of WO_3. *J. Mater. Sci*. **10,** 593–598 (1975).
43. Lalik, E., David, W. I. F., Barnes, P. & Turner, J. F. C. Mechanisms of reduction of MoO_3 to MoO_2 reconciled? *J. Phys. Chem. B* **105,** 9153–9156 (2001).
44. Jadczak, J. *et al.* Composition dependent lattice dynamics in $MoS_xSe_{(2-x)}$ alloys. *J. Appl. Phys*. **116,** 193505 (2014).
45. Feng, Q. *et al.* Growth of $MoS_{2(1-x)}Se_{2x}$ ($x = 0.41$–1.00) monolayer alloys with controlled morphology by physical vapor deposition. *ACS Nano* **9,** 7450–7455 (2015).

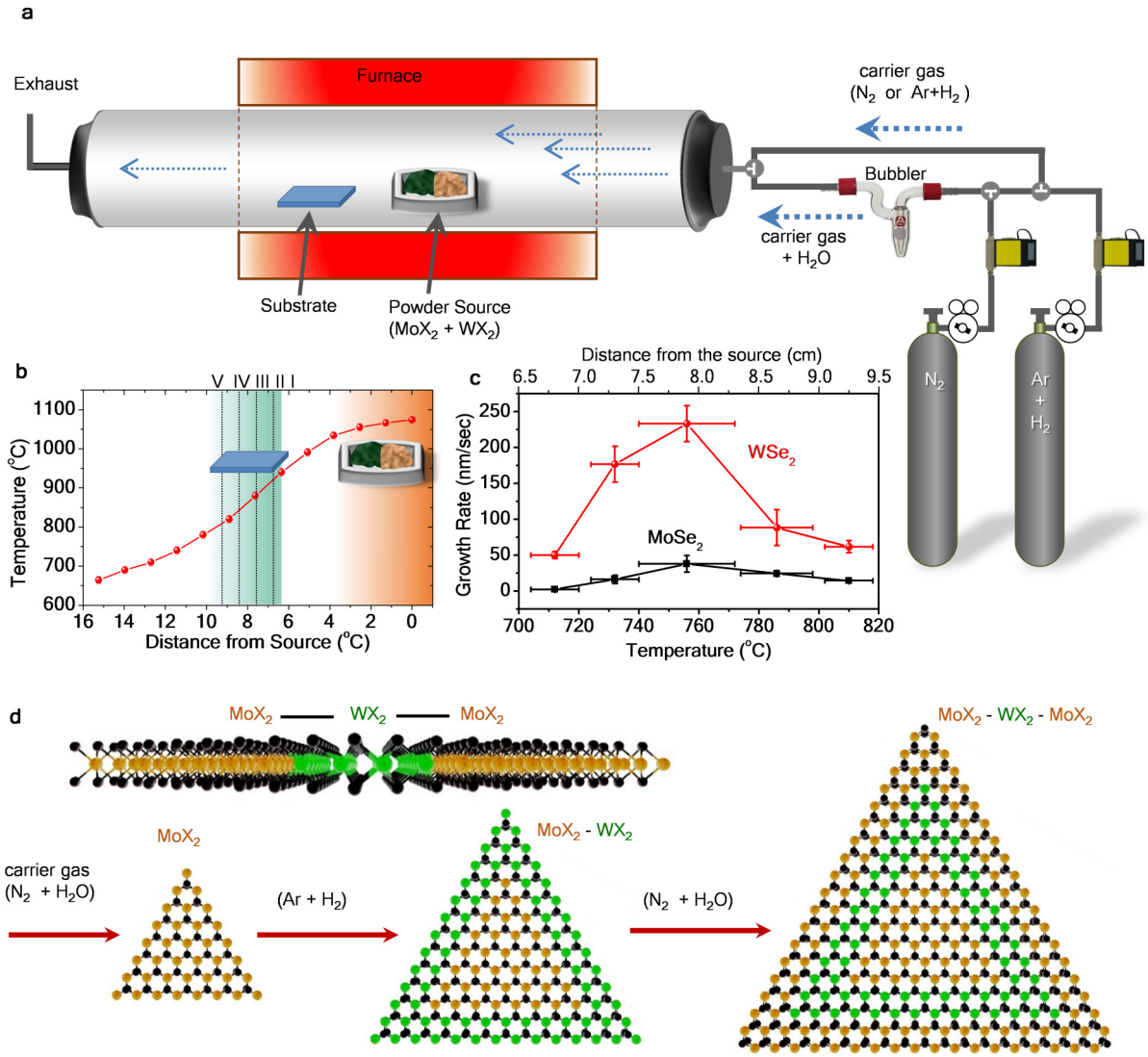

Extended Data Figure 1 | One-pot synthetic approach for sequential edge-epitaxy of TMDs. a, Schematics of the modified chemical vapour deposition system that allows the alternate switching of carrier gas that generates the selective edge-epitaxial growth for multi-junction heterostructure synthesis. Note that water vapour is introduced by passing the carrier gas through the bubbler. The carrier gas is selected by a three-way valve placed at the entrance of the quartz tube reactor. **b**, Temperature profile of the furnace, a single heterogeneous source containing both precursors is placed in the high-temperature zone, whereas the substrates are placed downstream at the lower-temperature zone. **c**, Growth rates for $MoSe_2$ and WSe_2 domains as a function of the substrate temperature. The error bars along the *y* axis denote the mean standard deviation ($\pm\delta$), and error bars along the *x* axis represent the average length of a typical growth region denoted in **b**. **d**, Atomic ball model, showing the material distribution across the heterostructure in cross-section (top) and plane view (bottom).

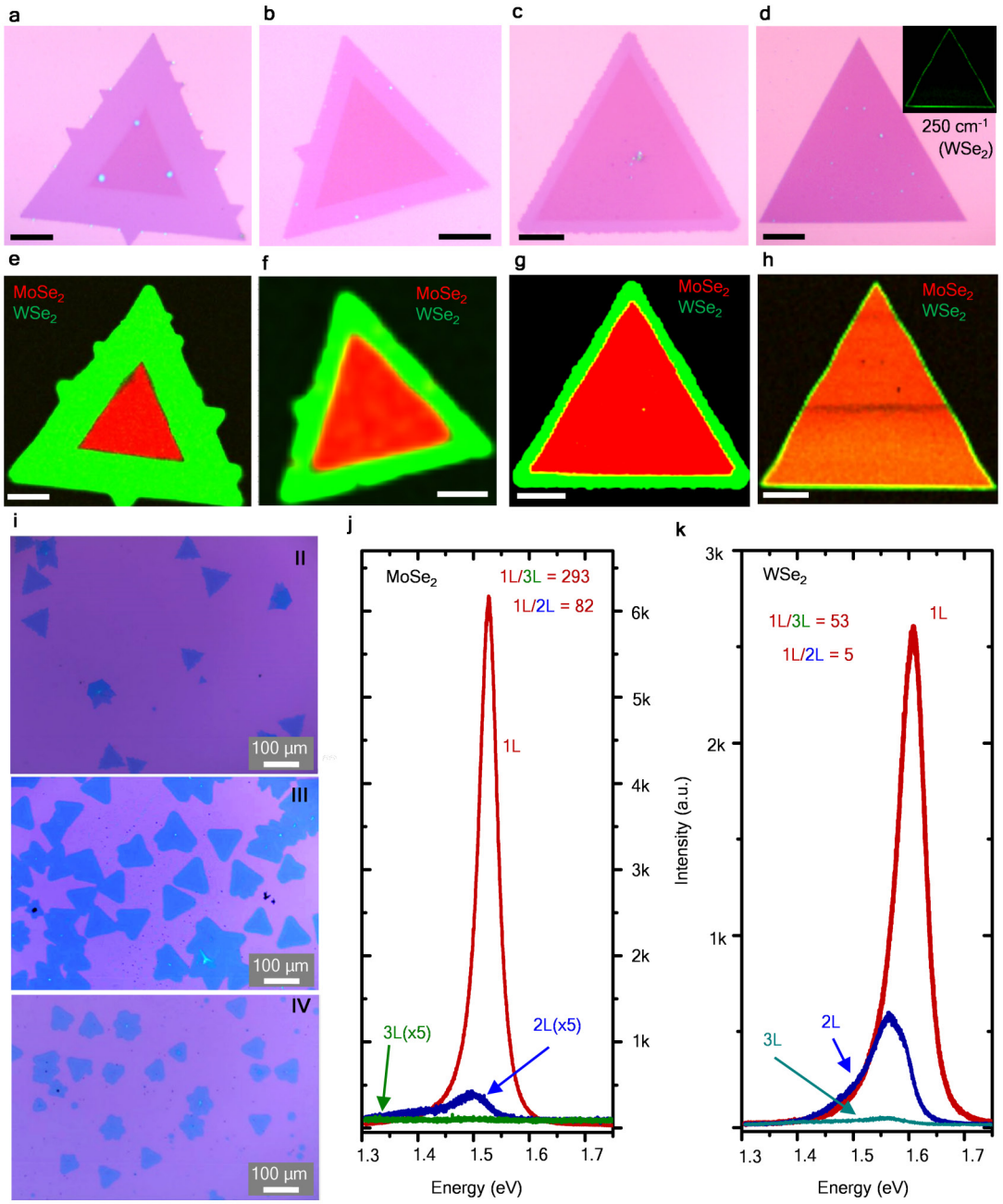

Extended Data Figure 2 | Growth of single-junction $MoSe_2$–WSe_2 lateral heterostructures. a–d, Optical images of single-junction $MoSe_2$–WSe_2 monolayer lateral heterostructures with different WSe_2 lateral growth times of 80 s (**a**), 45 s (**b**), 30 s (**c**) and 15 s (**d**). The inset in **d** shows the Raman map of the narrow WSe_2 shell, which is difficult to visualize in the optical image. **e–g**, Composite photoluminescence maps corresponding to optical images in **a–c**, respectively, at 1.53 eV ($MoSe_2$ domain) and 1.6 eV (WSe_2 domain). **h**, Composite Raman map corresponding to the optical image in **d**, at frequencies 240 cm^{-1} ($MoSe_2$ domain) and 250 cm^{-1} (WSe_2 domain). **i**, Low-magnification optical images of the $MoSe_2$–WSe_2 single-junction heterostructure shown in **b**, obtained at different distances from the source precursor as mentioned in Extended Data Fig. 1b, c (regions II to IV). **j**, **k**, Photoluminescence spectra of monolayer (1L), bilayer (2L) and trilayer (3L) heterostructures; $MoSe_2$ (**j**) and WSe_2 (**k**) domains. Scale bars: **a–h**, 10 μm.

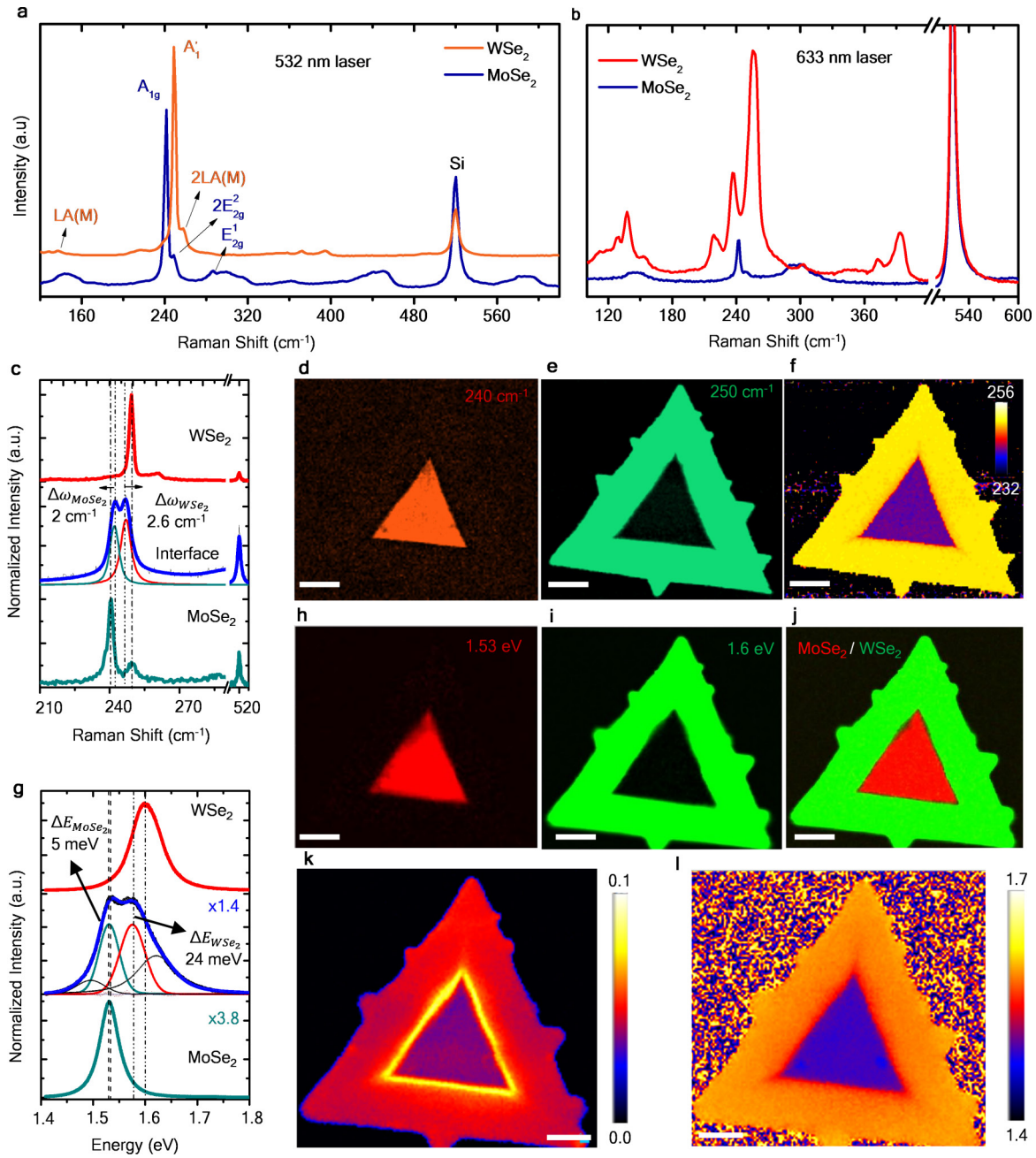

Extended Data Figure 3 | Optical properties of single-junction $MoSe_2$–WSe_2 lateral heterostructure. **a**, **b**, Raman spectra of $MoSe_2$ and WSe_2 domains from a single-junction $MoSe_2$–WSe_2 monolayer lateral heterostructure using 514 nm (**a**) and 613 nm (**b**) laser excitation. **c**, Raman spectra at the interfaces of the single-junction $MoSe_2$–WSe_2 lateral heterostructure. **d**, **e**, Composite Raman intensity maps at a frequency of 240 cm^{-1} ($MoSe_2$ domain, **d**), 250 cm^{-1} (WSe_2 domain, **e**). **f**, Position map corresponding to the optical image in Extended Data Fig. 2a. **g**, Photoluminescence spectra of $MoSe_2$, WSe_2 domains and at the interface of the $MoSe_2$–WSe_2 single-junction monolayer lateral heterostructure shown in Extended Data Fig. 2a. **h**–**j**, Photoluminescence intensity maps at 1.53 eV ($MoSe_2$ domain, **h**) and 1.6 eV (WSe_2 domain, **i**); the composite is shown in **j**. **k**, **l**, Peak width (in eV) map (**k**) and position (in eV) map (**l**) corresponding to the optical image in Extended Data Fig. 2a. Scale bars: **d**–**l**, 10 μm.

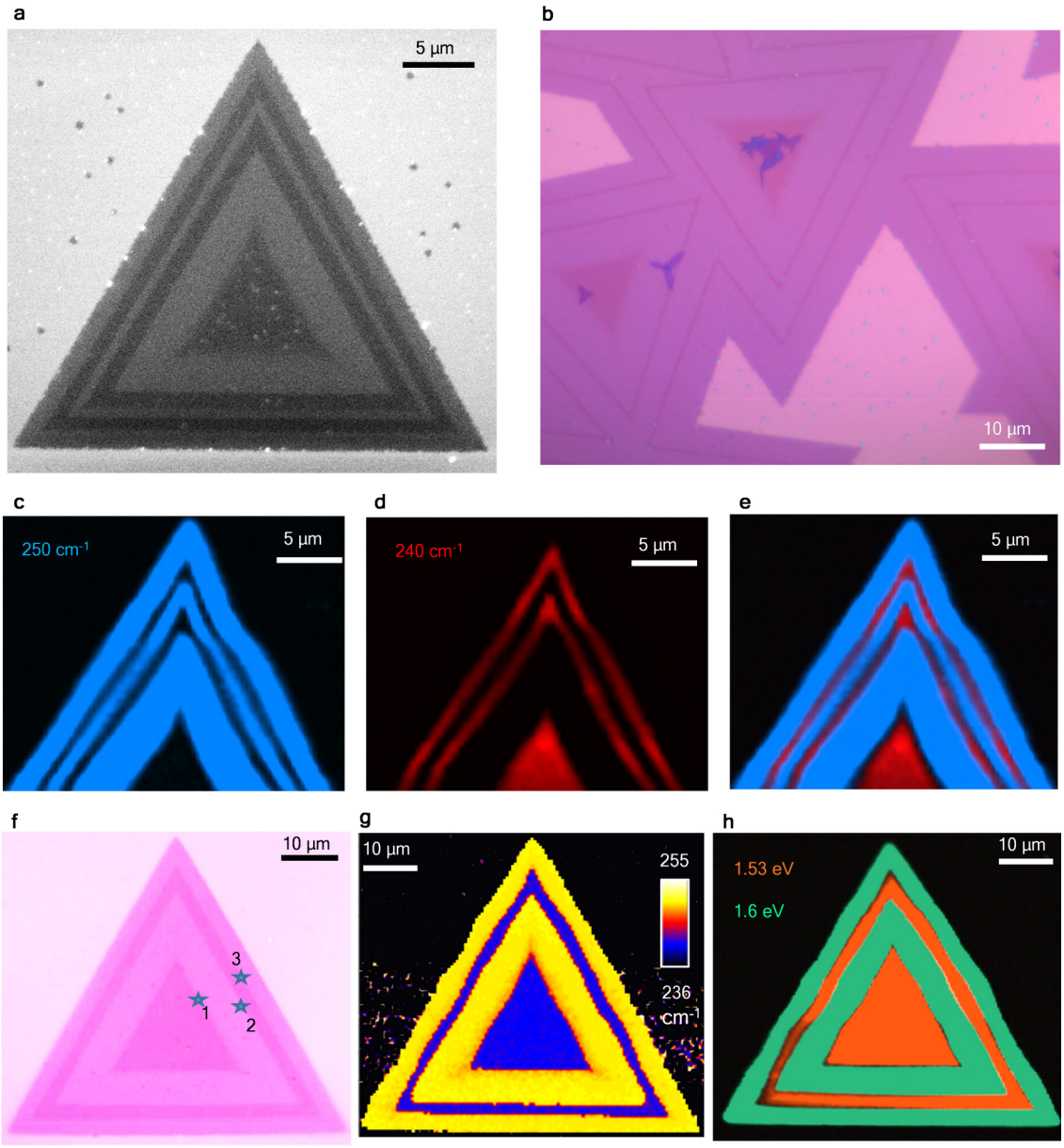

Extended Data Figure 4 | Optical properties of multi-junction $MoSe_2$–WSe_2 lateral heterostructure. **a**, Typical SEM image of a five-junction $MoSe_2$–WSe_2 monolayer lateral heterostructure corresponding to Fig. 1b. **b**, Optical microscope image of a large area of a five-junction $MoSe_2$–WSe_2 lateral heterostructure, corresponding to Fig. 1c showing the conformal growth of respective $MoSe_2$ or WSe_2 domains. **c**, **d**, Raman intensity map of five-junction $MoSe_2$–WSe_2 lateral heterostructure corresponding to Fig. 1b, g, at frequencies 250 cm^{-1} (**c**, WSe_2 domain) 240 cm^{-1} (**d**, $MoSe_2$ domain). **e**, Composite Raman map image at 250 cm^{-1} and 240 cm^{-1}. **f**, Optical image of a three-junction $MoSe_2$–WSe_2 monolayer lateral heterostructure corresponding to the inset of Fig. 1i. **g**, Raman peak position mapping between 236–255 cm^{-1}. **h**, Composite photoluminescence intensity mapping at 1.53 eV ($MoSe_2$ domain) and 1.6 eV (WSe_2 domain). Scale bars: **f**–**h**, 10 μm.

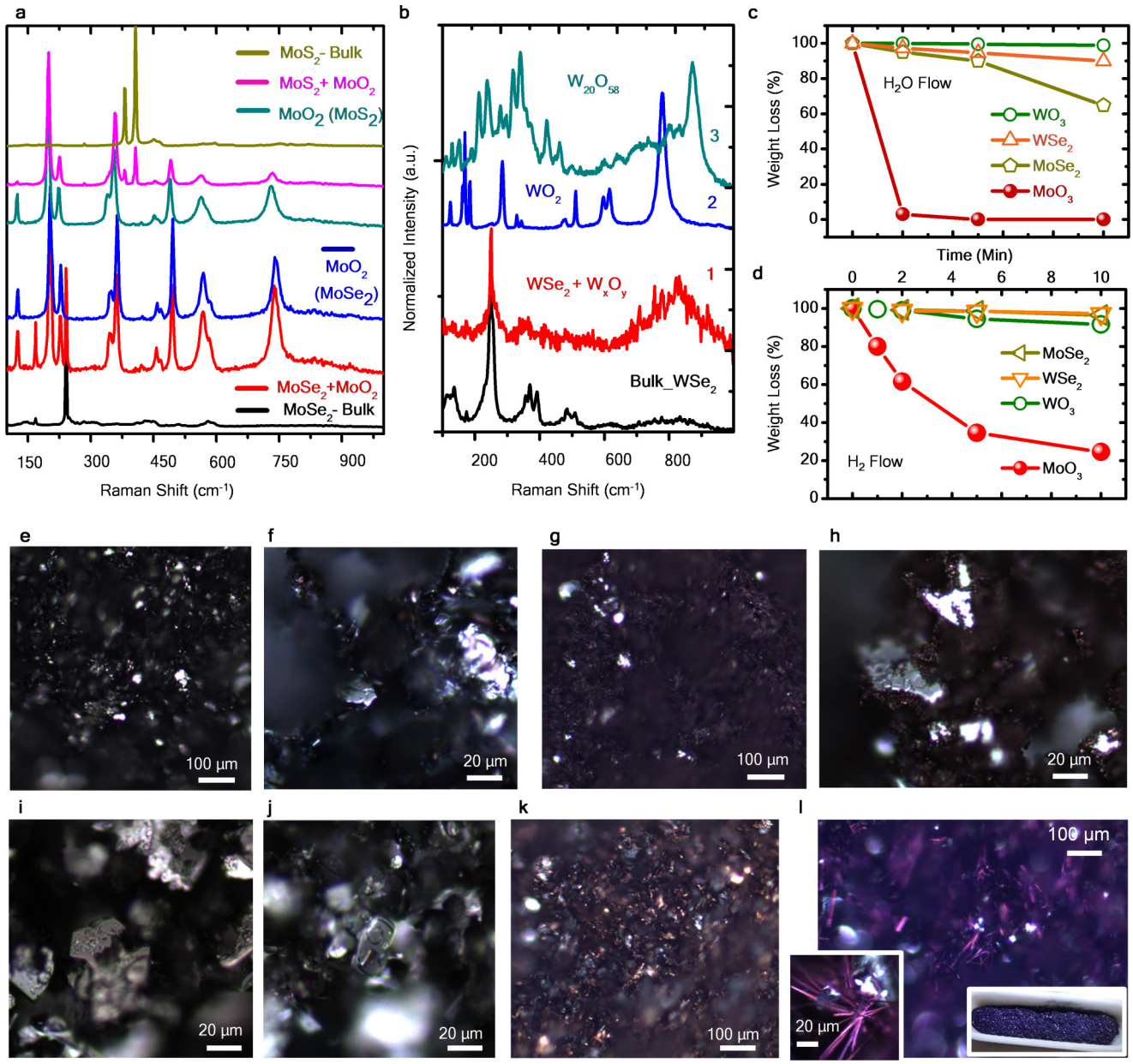

Extended Data Figure 5 | Effect of water vapour and H_2 on the solid sources (MoX_2 and WX_2). a, Raman spectral evolution of the MoO_2 oxide phase from both $MoSe_2$ and MoS_2 solid sources upon reaction with a constant flow of $N_2 + H_2O$ vapour for more than 20 min at 1,060 °C (Supplementary Table 2). **b**, Raman spectral evolution of different oxide phases of WX_2 upon reaction with different reactive gas environment for more than 20 min at 1,060 °C as follows. Only $Ar + H_2$ (5%) through H_2O (200 s.c.c.m.); the Raman spectra is composed of WSe_2, most likely a Se-deficient surface as well as a mixture of complex oxide phases as indicated by the broad peak around 800 cm^{-1} (1); first partially oxidized by $N_2 + H_2O$ (5 min) followed by $Ar + H_2$ (5%) through H_2O (200 s.c.c.m.) for 10 min. The dominant phase observed in the Raman spectra is WO_2[36–39,42] (2); completely oxidized by $N_2 + H_2O$ flow for 20 min—the dominant phase observed in the Raman spectra is $W_{20}O_{58}$ (3). **c**, **d**, Reduction of different metal oxide (MoO_3 and WO_3) and selenide ($MoSe_2$ and WSe_2) solid sources as a function of reaction time and carrier gases: in $N_2 + H_2O$ (**c**) and $Ar + H_2$ (5%) (**d**) flow conditions at 1,060 °C. It can be observed that the weight loss of MoO_3 (38.5% in 2 min) is very rapid compared to that of WO_3 (1% in 2 min). In contrast, the reduction rate of $MoSe_2$ and WSe_2 solid precursors are almost linear during H_2 exposure at high temperatures. During oxidation by H_2O, however, the weight loss of $MoSe_2$ is two and five times faster than that of WSe_2 and WO_3 respectively. **e**–**h**, A direct visualization of the reaction of $MoSe_2$ can be gained from the change in colour of the source precursor under different conditions: bulk powder of $MoSe_2$ (**e**); after reaction in $Ar + H_2$ (5%) through H_2O (200 s.c.c.m.) (**f**); after reaction in N_2 through H_2O (200 s.c.c.m.); the chocolate brown indicates the MoO_2 phase (**g**); the shiny surface indicates the presence of metallic molybdenum reduced from MoX_2 along with the MoO_2 phase (**h**). **i**–**l**, Different oxide phases of WX_2 upon reaction with different reactive gas environment for more than 20 min at 1,060 °C. Bulk powder of WSe_2 (**i**); only $Ar + H_2$ (5%) through H_2O (200 s.c.c.m.) (**j**, corresponding to spectrum 1 in **b**); first partially oxidized by $N_2 + H_2O$ (5 min) followed by $Ar + H_2$ (5%) through H_2O (200 s.c.c.m.) for 10 min (chocolate brown, **k**, corresponding to spectrum 2 in **b**)[36–39,42]; completely oxidized by $N_2 + H_2O$ flow for 20 min—the dominating phase observed in the Raman spectra is $W_{20}O_{58}$ (blue-violet, **l**, corresponding to spectrum 3 in **b**). The insets of **l** show the high magnification image (left) and the materials in an alumina boat (right).

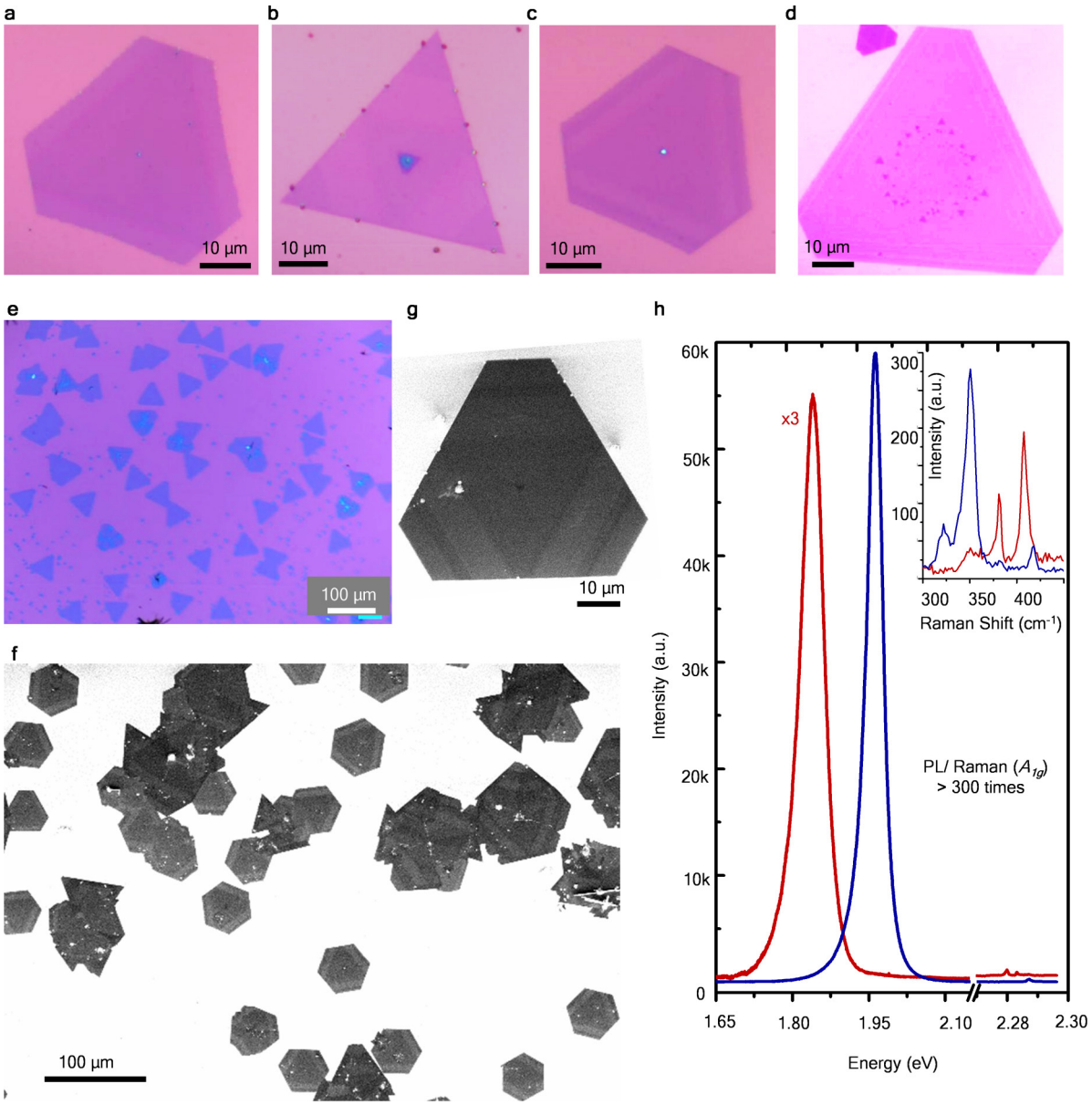

Extended Data Figure 6 | Growth of multi-junction MoS_2–WS_2 lateral heterostructure. a–**d**, Optical images of MoS_2–WS_2 monolayer lateral heterostructures: single-junction (**a**), two-junction (**b**), three-junction (**c**), five-junction (**d**). **e**, Typical low-magnification optical image of the five-junction structure shown in **d**. **f**, SEM images of the three-junction MoS_2–WS_2 lateral heterostructure shown in **c**. **g**, SEM image of a three-junction single island (Fig. 2b). **h**, Typical photoluminescence spectra from MoS_2 and WS_2 domains of the three-junction heterostructure shown in **g**. The strong photoluminescence intensity compared with that of the Raman A_{1g} mode (over 300 times greater) indicates the monolayer nature as well as high optical quality of the as-grown heterostructure.

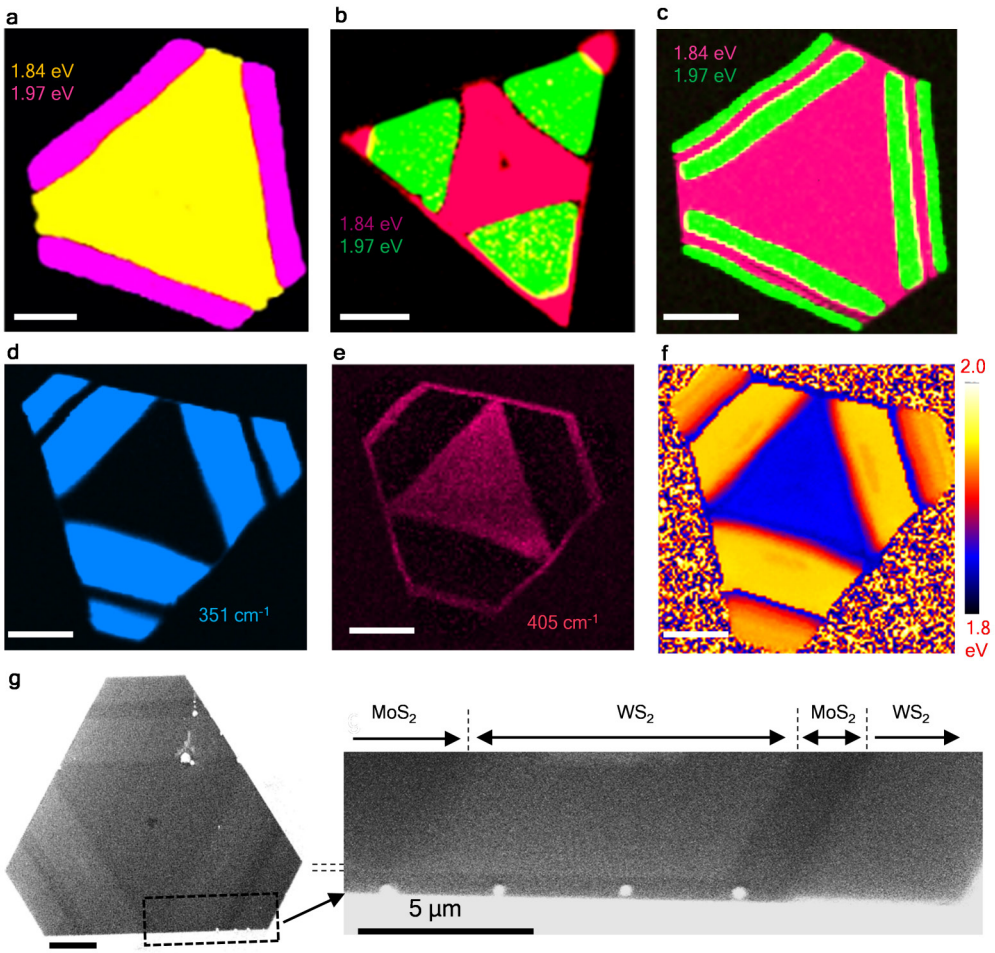

Extended Data Figure 7 | Optical properties of MoS_2–WS_2 lateral heterostructures. **a**–**c**, Composite photoluminescence intensity mapping of single-junction (**a**), two-junction (**b**) and three-junction (**c**) MoS_2–WS_2 monolayer lateral heterostructures corresponding to the optical images in Extended Data Fig. 6a–c, respectively, at 1.84 eV (MoS_2 domain) and 1.97 eV (WS_2 domain). **d**, Raman intensity mapping at frequency 351 cm^{-1} (**d**, WS_2 domain), 405 cm^{-1} (**e**, MoS_2 domain). **f**, Photoluminescence position mapping corresponding to the optical image in Fig. 2a. **g**, SEM image of a three-junction MoS_2–WS_2 monolayer lateral heterostructure island. The high magnification image of the boxed region, shown in the right panel, shows the lateral connectivity between respective domains of MoS_2 or WS_2. Scale bars: **a**–**g**, 10 μm.

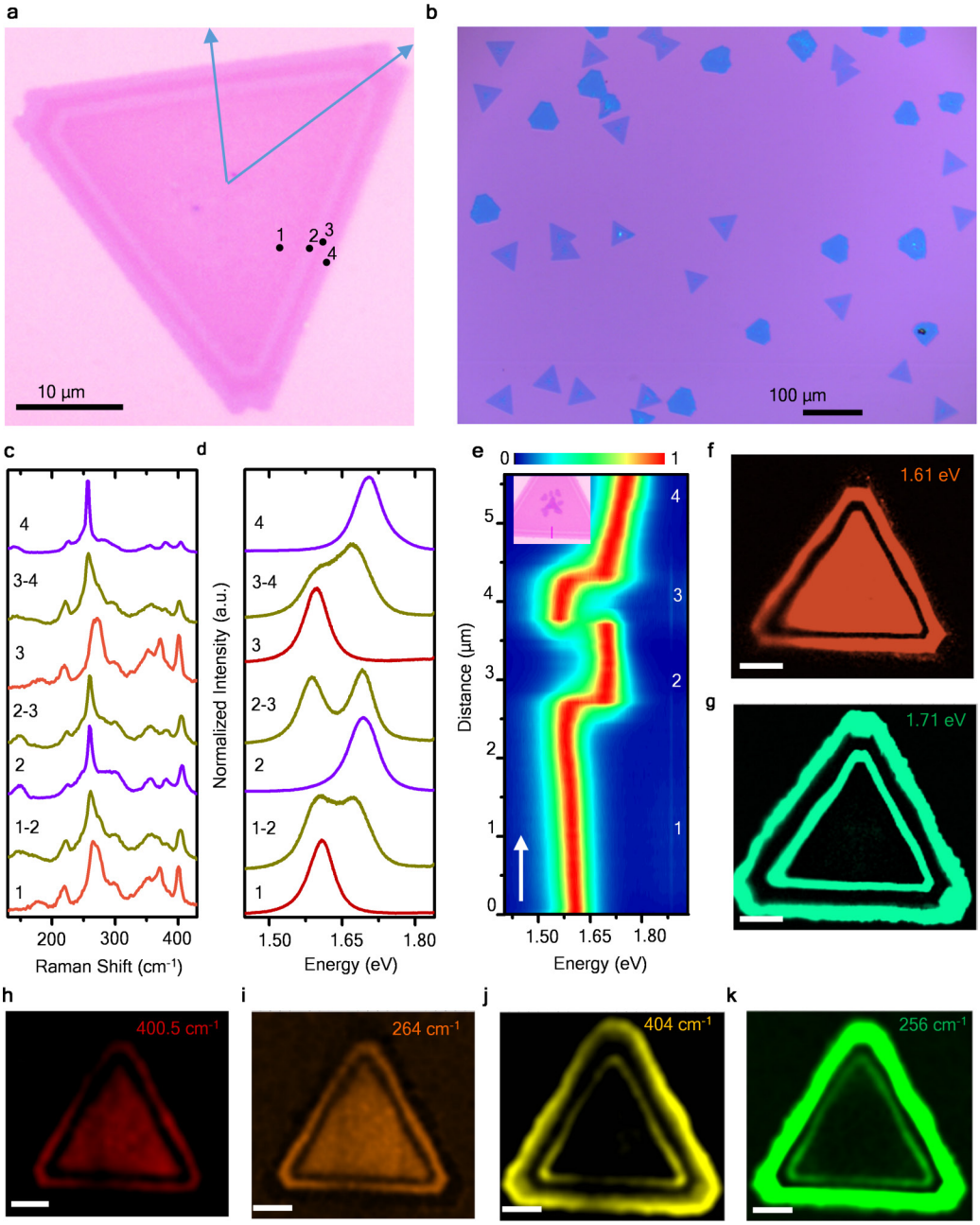

Extended Data Figure 8 | Growth of three-junction $MoS_{0.64}Se_{1.36}$ – $WSe_{1.32}S_{0.68}$ lateral alloy heterostructure. **a**, Optical image of a three-junction $MoS_{2(1-x)}Se_{2x}$–$WS_{2(1-y)}Se_{2y}$ monolayer lateral heterostructure. **b**, The corresponding low magnification optical image of the heterostructure shown in **a**. **c**, **d**, Raman (**c**) and photoluminescence (**d**) spectra corresponding to the optical image in **a** between points 1–4. **e**, Normalized photoluminescence contour colour plot along the direction perpendicular to the interfaces, as shown in the optical image in the inset. **f**, **g**, Photoluminescence intensity maps at 1.61 eV (**f**, $MoS_{0.64}Se_{1.36}$ domain) and 1.71 eV (**g**, $WSe_{1.32}S_{0.68}$ domain) corresponding to the optical image in Fig. 3a. **h**–**k**, Raman intensity maps (Fig. 3a) at frequency 400.5 cm^{-1} ($A_{1g(S–Mo)}$ modes, **h**); 264 cm^{-1} ($A_{1g(Se–Mo)}$ modes, **i**); 404 cm^{-1} ($A_{1g(S–W)}$ mode, **j**); and 256 cm^{-1} ($A_{1g(Se–W)}$ mode, **k**). Scale bars: **f**–**k**, 10 μm.

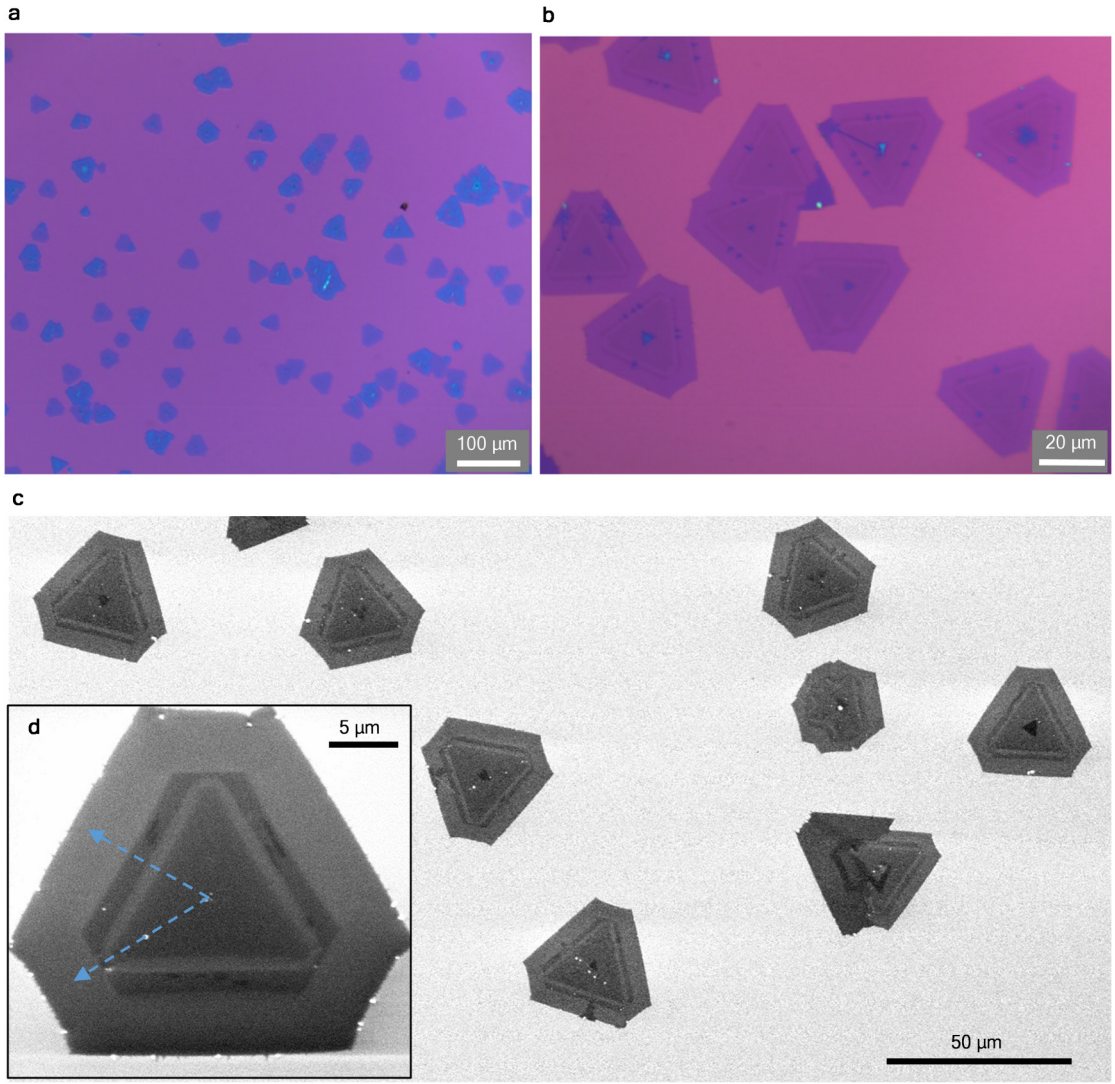

Extended Data Figure 9 | Growth of three-junction $MoSe_{0.96}S_{1.04}$–$WSe_{0.92}S_{1.08}$ lateral alloy heterostructure. a, **b**, Low-magnification optical images of three-junction $MoS_{2(1-x)}S_{2x}$–$WS_{2(1-y)}Se_{2y}$ monolayer lateral heterostructure (corresponding to the optical image in Fig. 3b). **c**, **d**, Typical large-area SEM image (**c**) and high magnification SEM image (**d**) of a single island showing the presence of different growth rates along the vertex and the axial directions. The $MoS_{2(1-x)}S_{2x}$ growth along the vertex direction is less than that of the axial direction.

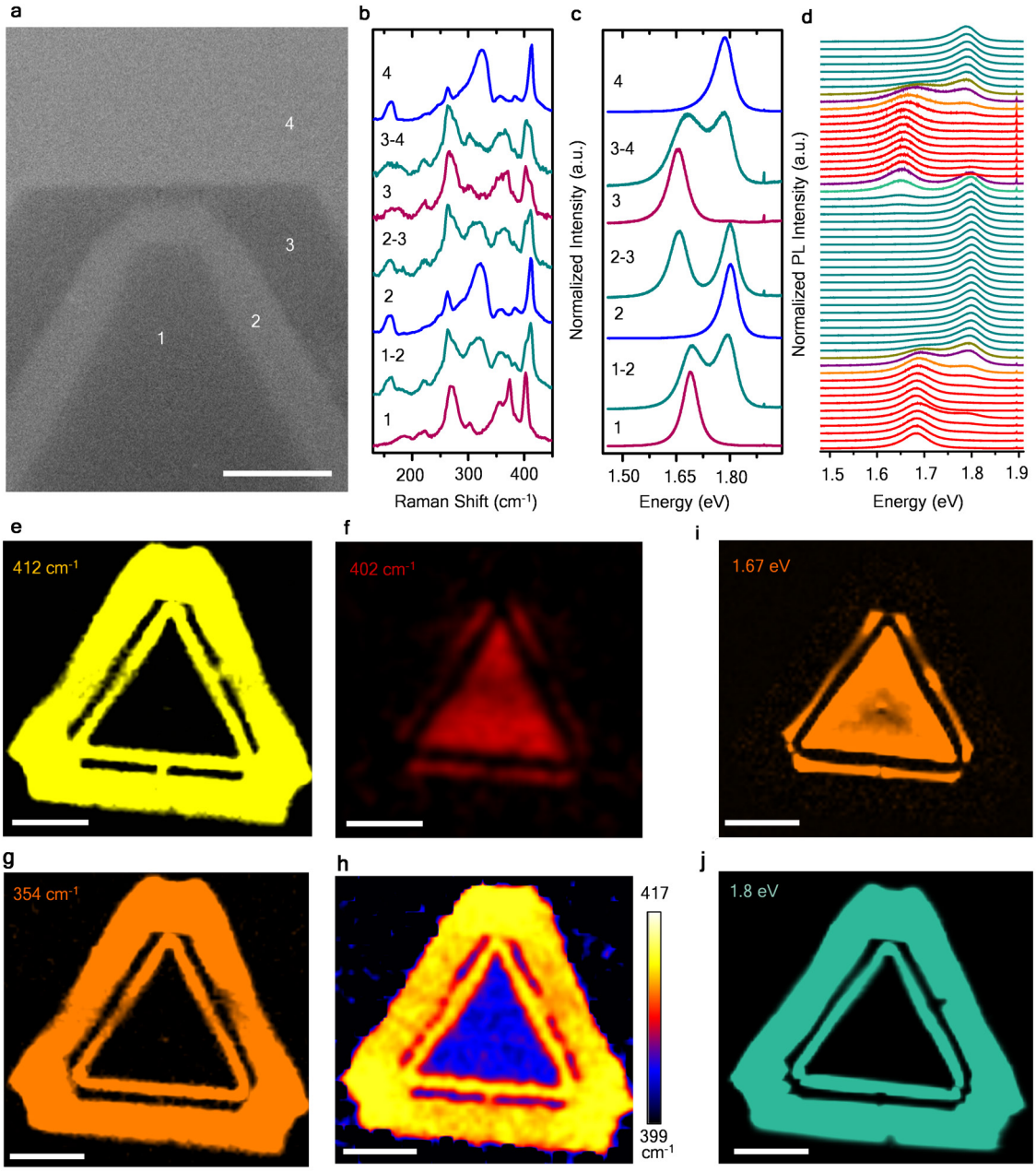

Extended Data Figure 10 | Optical properties of multi-junction $MoSe_{0.96}S_{1.04}$–$WSe_{0.92}S_{1.08}$ lateral heterostructure. **a**, SEM image of a three-junction $MoS_{2(1-x)}S_{2x}$–$WS_{2(1-y)}Se_{2y}$ monolayer lateral heterostructure. Scale bar, 2 μm. **b**, **c**, Raman (**b**) and photoluminescence (**c**) spectra of points 1 to 4; and interfaces. **d**, Normalized photoluminescence spectra from a line scan perpendicular to the three junctions, regions 1 to 4 in **a**, as indicated in the inset of Fig. 3e ($\lambda_{exc} = 633$ nm). **e**–**g**, Raman intensity maps corresponding to the optical image in Fig. 3b, at frequencies 412 cm^{-1} ($A_{1g(S-W)}$ modes, **e**); 402 cm^{-1} ($A_{1g(S-Mo)}$ mode, **f**) and 354 cm^{-1} ($E_{2g(S-W)}$ modes, **g**). **h**, Raman position mapping between 399–417 cm^{-1}. There is a thin line of $MoS_{2(1-x)}S_{2x}$ between the $WS_{2(1-y)}Se_{2y}$ strip along the vertex direction which could not be resolved during the Raman mapping. **i**, **j**, Photoluminescence intensity map, corresponding to the optical image in Fig. 3b, at 1.67 eV ($MoSe_{0.96}S_{1.04}$ domain, **i**) and 1.8 eV ($WSe_{0.92}S_{1.08}$ domain, **j**). Scale bars: **e**–**j**, 10 μm.